4

Solid State Research

1964

Prepared under Electronic Systems Division Contract AF 19(628)-500 by

Lincoln Laboratory

MASSACHUSETTS INSTITUTE OF TECHNOLOGY

Lexington, Massachusetts

The work reported in this document was performed at Lincoln Laboratory, a center for research operated by Massachusetts Institute of Technology, with the support of the U.S. Air Force under Contract AF 19(628)-500.

4

Solid State Research

1964

Issued 23 March 1965

Lincoln Laboratory

MASSACHUSETTS INSTITUTE OF TECHNOLOGY

Lexington, Massachusetts

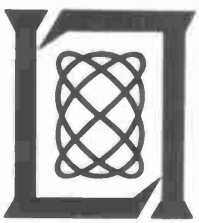

ABSTRACT

This report covers in detail the solid state research work at Lincoln Laboratory for the period 1 October 1964 through 31 December 1964. The topics covered are Solid State Device Research, Laser Research, Materials Research, Band Structure and Spectroscopy of Solids, and Magnetism and Resonance.

Accepted for the Air Force
Stanley J. Wisniewski
Lt Colonel, USAF
Chief, Lincoln Laboratory Office

INTRODUCTION

I. SOLID STATE DEVICE RESEARCH

Coherent emission at 5.2 microns parallel to the direction of the diode current has been obtained in n^+pp^+ InSb diodes. Large-volume luminescence and coherent emission in similar n^+pp^+ InSb diodes were described in the last quarterly progress report, but the coherent beam was emitted perpendicular to the direction of current, as in all other existing semiconductor lasers. However, the large active regions of these InSb diodes, in which lifetimes of 10^{-7} to 10^{-6} sec permit population inversion in regions of the order of 100 microns away from the injecting contacts, are naturally suited for laser oscillations longitudinal to the current. Such lasers are free from some of the structural restrictions of the perpendicular lasers; for example, they can be more readily constructed in arrays. They also promise to emit coherently over large areas, hence with small beam angles, and they should be suited for large power outputs. Coherent emission was obtained near 10°K with 50-nsec current pulses of 20 amp (6×10^4 amp cm^{-2}), with a minimum longitudinal magnetic field of 7 kgauss. Comparison of the wavelength and the magnetic shift with earlier data on InSb diodes indicates that the highest energy state of the spin-split lowest Landau level is involved in the transition. Mode structure was observed with mode spacing of 120 Å as expected from the 220-micron length of the longitudinal cavity.

The PbSe diode laser, with a coherent emission peak at 8.5 microns at 12°K, has been further developed. Fabrication techniques are based on controlling carrier type and concentration by adjusting the Pb:Se ratio, rather than adding impurities. The diode emission below threshold exhibits two spectral peaks, one with a maximum near 8.5 microns which increases superlinearly with current, and another with a maximum at 10.1 microns which increases slowly with current. Laser action associated with the 8.5-micron peak occurs above a threshold current density of 2000 amp cm^{-2}. The unresolved emission peak shifts linearly to higher energies with a magnetic field oriented in the <100> direction at the rate of 7.1×10^{-8} ev/gauss, or 17 Mcps/gauss, which is the expected value if the emission is associated with band-to-band transitions. The threshold current density decreases to a fraction of its zero field value in a magnetic field of approximately 10 kgauss, then rises slowly with increasing field. The PbSe laser should eventually be of particular interest for communications since its emission is in the 8- to 14-micron atmospheric window, a spectral region of high atmospheric transparency where attenuation due to scattering by haze is generally low.

II. LASER RESEARCH

The frequency, far-field, and intensity characteristics of stimulated Brillouin emission at 90° to the ruby laser beam in nitrobenzene have been measured. The observed Brillouin frequency shift is consistent with that measured for 90° Brillouin scattering of a He-Ne laser in nitrobenzene.

Further etalon studies of the stimulated Raman emission at 90° have shown the presence of many on-axis Raman cavity modes as well as a continuum of walkoff modes, all within a few cm^{-1} bandwidth.

Theoretical studies of the stimulated Stokes and anti-Stokes radiation from a point source predict exponential growth of a spherical Stokes wave, and exponential damping of anti-Stokes radiation in all directions including that of phase matching. However, the anti-Stokes radiation will be emitted near a boundary of the Raman medium.

Two-photon absorption effects were observed in the photoelectron current of a multiplier illuminated by a focused CW infrared He-Ne laser. Unusual photoconduction effects, partly attributable to two-photon absorption, were observed in several samples of large-gap, high-resistivity materials illuminated by a spiking ruby laser.

Measurements of the amplitude noise of a stable He-Ne laser have shown good agreement with bandwidth and noise intensity predictions of a van der Pol oscillator theory for above threshold data and a linear maser amplifier theory for below threshold data.

Stable pulsed arc discharge conditions have been achieved in the high-pressure mercury system to obtain an estimated single pass gain of 0.3 percent. A sufficiently low loss optical cavity is being assembled for obtaining laser oscillation.

III. MATERIALS RESEARCH

Single crystals of sapphire (melting point 2050°C) have been grown by the Czochralski method in a resistance furnace that was recently developed for operation in oxidizing, neutral, or reducing atmospheres at temperatures up to 2400°C. The melt was contained in an iridium or molybdenum crucible under an argon atmosphere. Since the molten sapphire did not evaporate appreciably, it was possible to remove the zirconia tube used to protect the tantalum heater element from oxygen and other reactive gases.

Additional experiments on the vapor growth of iodine crystals by forced convection have provided further confirmation that constitutional supercooling of the vapor occurs at sufficiently high growth velocities. Additional data have been obtained on the variation of growth velocity with the temperature difference between the source of iodine vapor and the growing interface. These data are fitted satisfactorily by an equation derived from elementary boundary layer theory.

Single crystals of Ti_2O_3 (~1 cm^3) and TiO (~1 mm^3) have been grown by the Czochralski method in the resistance furnace used for sapphire growth. Large-grained boules of Ti_2O_3 have been obtained by the Verneuil method with an induction plasma torch. Measurements of the Seebeck coefficient have been made on a single crystal of Ti_2O_3 between 7° and 550°K.

Hall coefficient (R_H) measurements have been made at 77°K on several samples of In_4SbTe_3. Application of the one-carrier expression $n = -1/R_H e$ gives electron concentrations of 1.1 and 1.2×10^{22} cm^{-3} for two high-pressure samples and 8.8, 9.0 and 9.4×10^{21} cm^{-3} for three low-pressure samples. These results indicate that the difference in superconducting behavior between high- and low-pressure samples may be due to a difference in carrier concentrations.

The partial pressures of Hg(g) and Te_2(g) in equilibrium with Hg-saturated HgTe(c), Te-saturated HgTe(c), and some Hg-Te melts between about 400° and 700°C have been determined by measuring the optical density of the vapor as a function of wavelength. The partial pressures depend strongly on the composition of the solid phase. The Gibbs free energy of formation of HgTe(c) from Hg(g) and Te_2(g) is found to be $\Delta G° = -41.66 + 42.71(10^{-3})T$ kcal/mode.

Wet chemical methods have been developed for determining Hg and Te in HgTe with an accuracy of about 1 part per thousand and for determining In, Sb and Te in 0.2 g In-Sb-Te samples with an accuracy of about 2 parts per thousand for each component.

IV. BAND STRUCTURE AND SPECTROSCOPY OF SOLIDS

The study of the interband transitions in antimony initially reported in the last quarter has been further extended. The most probable locations in momentum space of the energy minima involved in the interband transitions have been deduced and the reduced effective masses and energy gaps have been obtained. It has also been found that the energy bands are nonparabolic. In order to more fully appreciate these results, the dispersion relations for the relevant points in the Brillouin zone have been developed in terms of the $\vec{k} \cdot \vec{p}$ Brillouin-Wigner perturbation theory and the symmetry properties. The nonparabolic character of the energy bands is incorporated in this development; furthermore, it is possible to include the effects of spin-orbit interaction in this formalism.

In another related problem, the magnetoplasma effects in bismuth are being investigated in detail. Studies on this semimetal offer the advantage that the contributions due to interband effects should be negligible near the plasma frequencies. Thus, this work should serve as a guide in interpreting the more complex effects observed in antimony where the interband and intraband effects are coupled to each other.

The Faraday rotation in the energy region of the indirect transition in germanium is being studied at high magnetic fields; oscillatory effects due to the exciton and also due to transitions from the valence band to the electronic Landau ladder of the conduction band have been observed. Since Faraday rotation is a dispersive effect, contributions due to the direct and indirect transitions are superimposed and thus a direct comparison of the matrix elements involved in the respective transitions can be made.

In GaSb the study of the magnetoabsorption due to exciton complexes, believed to consist of an ionized acceptor ion and an exciton, has been extended to 90 kgauss. It has been found that the functional behavior of the diamagnetic shift changes at magnetic fields above ~20 kgauss and tends to a linear behavior; this is in agreement with the theory of Elliott and Loudon. In a related theoretical development of the optical absorption due to excitons, the theory of Elliott, which holds in the limit of small wave vector, has been extended to the more general case of finite wave vector.

The magnetic field dependence of the photoluminescence of GaAs has been studied for both n- and p-type material. In n-type material the exciton lines, as well as the transitions proceeding through holes trapped at acceptors, exhibited a quadratic behavior at low fields which

eventually became linear at high fields, and intensities which were independent of magnetic field. This type of energy shift can be accounted for by a simple effective mass hydrogenic model; however, hole spin splittings which were expected on the basis of previous experiments were not observed. In p-type materials an additional strong line was observed; as the magnetic field was increased this line shrank in intensity, while the other lines grew, sometimes by as much as one order of magnitude.

In an attempt to resolve the polaron anomaly in CdS, a Fröhlich-type Hamiltonian with an isotropic electron-phonon interaction term is being used as a model to calculate the piezoelectric electron-phonon coupling. The effects of such coupling on the electron energy are being investigated at zero temperature where the lowest order perturbation theory can be rigorously evaluated unlike the Hopfield-Mahan calculation which required severe approximations. Very preliminary results indicate that, at magnetic field strengths of several kgauss, this model yields a piezoelectric interaction which is much too weak to account for the experimental results.

In connection with the band structure of the rare earth metals, a formal solution of the relativistic Schrödinger equation has been obtained for a periodic "muffin tin" potential, using the augmented plane-wave technique. The problem does not appear to be much more difficult than that of evaluating the nonrelativistic problem. The principal source of inaccuracies remains the same, namely, the lack of precision in the assumed potential. Since this technique appears feasible, the programming of the calculation to obtain the energy bands of specific materials is now being considered.

The study of deep impurities, such as sulfur, in silicon is continuing. The behavior under stress of the transitions between the ground state of an impurity center and its excited p-like states has been examined. It has been found that all transitions behave identically under stress and that this is consistent with a simple deformation potential model. An analysis of the results has yielded a pure shear deformation potential of 7.9 ± 0.2 ev.

Galvanomagnetic measurements have been made on newly grown HgTe. In some samples, at 4°K, Hall mobilities larger than those found in InSb have been measured. Both n- and p-type material have been studied; magnetoresistance, magneto-Hall effects, and the electron Hall mobility have been measured at 4° and 78°K in fields up to 105 kgauss. Magnetoresistance ratios of up to 200 have been observed. Attempts are being made to fit the data to a mixed conduction model. The Hall coefficient as a function of temperature has been employed to obtain a value for the thermal energy gap E_t in HgTe, using an analysis similar to that used in HgSe. The value obtained is $E_t = -0.02 \pm 0.01$ ev.

V. MAGNETISM AND RESONANCE

Calculations of the Curie temperature in cubic spinels by means of a new high-temperature expansion have been completed and compared with results by older methods. The improvement is marked for the case of zero B-B interactions, but is pronounced for nonzero B-B interactions.

It has been pointed out that the Overhauser-Stearns conclusion from their Mossbauer measurements on Fe-Al alloys is premature because the plane-wave approximation for the conduction electrons is not good in the vicinity of the nucleus. If the plane wave is orthogonalized to the core electrons for determining the value of the wave function at the nuclear positions, the spin density of the conduction electrons that is induced by the localized electrons is in much better accord with experiment. It was shown qualitatively that corrections to the other approximations in the Ruderman-Kittel theory also improve the agreement.

The need for improved materials for digital phase shifters for radar-antenna arrays has motivated a reinvestigation of the conditions for achieving spontaneously square B-H loops in ferrites. It was shown that reverse-domain nucleation may occur either at a grain boundary or at a chemical inhomogeneity having roughly 0.1 a grain volume, a magnetization about 2 percent different from the parent matrix, and no static crystallographic discontinuity at the inhomogeneity matrix interface. Evidence has been found for the existence of such chemical inhomogeneities in square-loop ferrites containing small concentrations of Jahn-Teller ions.

Susceptibility, anisotropy, and resonance data for the ilmenites $FeTiO_3$ and $CoTiO_3$ have been reconciled by the assumption that the spin-orbit splitting is larger than the trigonal-field splitting.

Single crystals of ReO_3 have been prepared and found to be metallic with a room-temperature resistivity of 8×10^{-6} ohm-cm.

The perovskite $LaCoO_3$ was found to exhibit a first-order rhombohedral $\rightleftarrows$ rhombohedral phase change at 1210°K, and the crystallographic data appear to support the creation of two cobalt sublattices below 1210°K, on one of which the cobalt ions are primarily in a low-spin state and on the other in a high-spin state. The details of the low-spin $\rightleftarrows$ high-spin distribution as a function of temperature are not yet firmly established.

Crystallographic and magnetic studies of the systems $Fe_xMn_{1-x}P$ and FeP-FeAs-FeSb have been initiated. In the first system the metamagnetic $\rightleftarrows$ ferromagnetic transition increases with x to reach the Curie temperature at about $x = 0.25$. Within the range $0.8 < x < 1.0$ there is a change from metamagnetism to ferromagnetism.

Two main areas are being investigated for the improvement of measurements using phonon generation at 70 Gcps: thin-film transducers and the reduction of receiver noise. The system is also being modified to permit measurements down to 1.5°K.

TABLE OF CONTENTS

ORGANIZATION

SOLID STATE DIVISION

H. C. Gatos, *Head*
A. L. McWhorter, *Associate Head*
P. E. Tannenwald, *Assistant Head*
M. J. Hudson, *Assistant*
D. T. Stevenson*
R. H. Kingston†

GROUP 81
SEMICONDUCTOR PHYSICS

J. M. Honig, *Leader*
T. C. Harman, *Assistant Leader*

Argyres, P. N.
Brebrick, R. F.
Dresselhaus, G. F.
Duston, D. K.‡
Gardner, M.
Groves, S. H.
Hilsenrath, S.
Houghton, B. H.*
Kelley, P. L.
Kleiner, W. H.
Mason, V. J.
Paladino, A. E.
Rawson, N. B.*
Trent, P. H.
Van Zandt, L. L.

GROUP 82
MAGNETISM AND RESONANCE

J. B. Goodenough, *Leader*
H. J. Zeiger, *Associate Leader*

Arnott, R. J.
Bermon, S.
Burke, J. W.
Delaney, E. J.
Dwight, K., Jr.
Feinleib, J.
Feldman, B.
Ferretti, A.
Germann, R. W.
Kaplan, T. A.
Kern, S.
Kernan, W. C.
Menyuk, N.
Newman, W. A.
Parker, C. D.
Perry, F. H.
Raccah, P. M.
Ridgley, D. H.
Rogers, D. B.
Stanley, H. E.*
Stickler, J. J.
Thaxter, J. B.
Weber, R.
Weinberg, D. L.
Whipple, E. R.

GROUP 83
ELECTRONIC MATERIALS

E. P. Warekois, *Leader*
A. J. Strauss, *Assistant Leader*

Andrews, H. I.‡
Bachner, F. J.‡
Banus, M. D.
Button, M. J.
Cornwell, J. C.
Ehlers, H. H.
Fahey, R. E.
Farrell, L. B.
Finn, M. C.
Fischler, S.
Giardino, N. A.
Kafalas, J. A.
LaFleur, W. J.
Lavine, M. C.*
Owens, E. B.
Plonko, M. C.
Reed, T. B.
Roddy, J. T.
Siuta, V. P.‡
Vernon, S. D.‡

GROUP 84
SOLID STATE SPECTROSCOPY

J. G. Mavroides, *Leader*
G. B. Wright, *Assistant Leader*

Carman, R. L.*
Curran, E. A.
Dickey, D. H.
Dimmock, J. O.
Dresselhaus, M. S.
Edwards, D. F.
Fulton, M. J.
Halpern, J.
Johnson, E. J.
Kolesar, D. F.
Krag, W. E.
Larsen, D. M.
Mason, W. C.
Mastromattei, E. L.
Scouler, W. J.
Strahm, N. D.‡
Walters, E.

GROUP 85
APPLIED PHYSICS

R. H. Rediker, *Leader*
R. J. Keyes, *Assistant Leader*

Bates, D. H.
Butler, J. F.
Calawa, A. R.
Carter, F. B.
Caswell, F. H.
Clough, T. F.
Donaldson, P. L.
Foyt, A. G.§
Grant, C. R.
Hinkley, E. D.
Hurwitz, C. E.
McPhie, J. M.
Melngailis, I.
Nill, K. W.‡
Palermo, J. S.
Phelan, R. J., Jr.
Quist, T. M.
Stopek, S.
Sullivan, F. M.
Walpole, J. M.‡
Ward, J. H. R., III
Youtz, P.

GROUP 86
OPTICS AND INFRARED

F. L. McNamara, *Acting Leader*
M. M. Litvak, *Assistant Leader*

Billups, R. R.
Bostick, H. A.
Carbone, R. J.
Chatterton, E. J., Jr.
Dennis, J. H.
DiMarzio, E. W.
Freed, C.
Longaker, P. R.
Merrill, E. R.
O'Connor, J. R.
Pitts, R. F.
Rotstein, J.
Sinclair, R. S.
Soref, R. A.
Underwood, D. I.
Wong, G. W.
Ziegler, H. L.
Zieman, H. E.
Zimmerman, M. D.

---

* Part Time
† Leave of Absence
‡ Research Assistant
§ Staff Associate

REPORTS BY AUTHORS ENGAGED IN SOLID STATE RESEARCH

15 October 1964 through 15 January 1965

PUBLISHED REPORTS

Journal Articles*

JA No.			
2366	Spontaneous Bending of Thin {111} Crystals of III-V Compounds	M. C. Finn H. C. Gatos	Surface Sci. 1, 361 (1964)
2370	Theory of Electromagnetic Field Measurement and Photoelectron Counting	P. L. Kelley W. H. Kleiner	Phys. Rev. 136, A316 (1964)
2374	Aspherical Spin-Density in S-State Cations	T. A. Kaplan	Phys. Rev. 136, A1636 (1964)
2380A	Optical deHaas-Shubnikov Effect in Antimony	M. S. Dresselhaus J. G. Mavroides	Solid State Commun. 2, 297 (1964)
2383	Partial Pressures and Gibbs Free Energy of Formation for Congruently Subliming CdTe(c)	R. F. Brebrick A. J. Strauss	J. Phys. Chem. Solids 25, 1441 (1964)
2413A	Band Structure of HgTe and HgTe-CdTe Alloys	T. C. Harman W. H. Kleiner A. J. Strauss G. B. Wright J. G. Mavroides J. M. Honig D. H. Dickey	Solid State Commun. 2, 305 (1964)
2420A	Evidence of Stimulated Emission in Ruby-Laser-Pumped GaAs	J. J. Schlickman M. E. Fitzgerald R. H. Kingston	Proc. IEEE (Correspondence) 52, 1739 (1964)
2423	Constitutional Supercooling in Iodine Vapor Crystal Growth	T. B. Reed W. J. LaFleur	Appl. Phys. Letters 5, 191 (1964)
2453	A Solid-State Room-Temperature Operated GaAs Laser Transmitter	G. F. Dalrymple† B. S. Goldstein† T. M. Quist	Proc. IEEE (Correspondence) 52, 1742 (1964)
2486	Band Structure and Magnetism of Gadolinium Metal	J. O. Dimmock A. J. Freeman‡	Phys. Rev. Letters 13, 750 (1964)

* Reprints available.

† Division 4.

‡ Author not at Lincoln Laboratory.

UNPUBLISHED REPORTS

Journal Articles

JA No.			
2443	Electric Furnace for Operation in Oxidizing, Neutral, and Reducing Atmospheres to 2400°C	T. B. Reed R. E. Fahey	Accepted by Rev. Sci. Instr.
2456	Pressure Dependence of the Ag_2Se α-β Transition Temperature	M. D. Banus	Accepted by Science
2457	Magnetic Properties of InAs Diode Electroluminescence	F. L. Galeener* I. Melngailis G. B. Wright R. H. Rediker	Accepted by J. Appl. Phys.
2460	Electrical Properties of Ferromagnetic CrO_x ($1.89 < x < 2.02$)	D. S. Chapin J. A. Kafalas J. M. Honig	Accepted by J. Phys. Chem.
2464	Semiconductor Lasers	R. H. Rediker	Accepted by Phys. Today
2474	Optical Pyrometer Measurement of RF Power	T. B. Reed J. T. Roddy	Accepted by Rev. Sci. Instr.
2475	Simple Construction for Determining the Phase Change of Light Reflected at Normal Incidence	G. B. Wright	Accepted by Appl. Optics
2477	Magnetoabsorption of the Indirect Transition in Germanium	J. Halpern B. Lax	Accepted by J. Phys. Chem. Solids
MS-985A	Experiments on Room Temperature Nernst-Ettingshausen Refrigerators	T. C. Harman J. M. Honig S. Fischler A. E. Paladino M. J. Button	Accepted by Trans. ASME

Meeting Speeches†

MS No.			
1110A	Principles of Injection Lasers	R. H. Rediker	Symposium on Optical and Electro-Optical Information Processing Technology, Boston, 9-10 November 1964

* Author not at Lincoln Laboratory.

† Titles of Meeting Speeches are listed for information only. No copies are available for distribution.

Unpublished Meeting Speeches (Continued)

MS No.			
1124	Engineering Design Factors in Tetrahedral-Anvil-Hinge High Pressure Equipment	A. R. Leyenaar* M. D. Banus	ASME Symposium on High Pressure Technology, New York, 30 November 1964
1132	Automatic Potentiometric EDTA and Redox Titrations of Nonstoichiometric Compounds	M. C. Gardels J. C. Cornwell	Twelfth Anachem Conference, Detroit, Michigan, 21-23 October 1964
1134	Chemical Uses of Induction Plasmas	T. B. Reed	AIChE Symposium on High Temperature Processes, Boston, 7-10 December 1964
1167	PbSe Diode Laser	J. F. Butler A. R. Calawa R. H. Rediker	1964 Electron Devices Meeting, Washington, D. C., 29-31 October 1964
1222	Present and Future of Laser Devices	R. H. Rediker	
1172	An Investigation into Eddy-Current Induced Non-Destructive Readout in Thin Film Memories	M. S. Maltz	Conference on Magnetism and Magnetic Materials, Minneapolis, Minnesota, 16-19 November 1964
1174	Complex vs Band Formation in Perovskite Oxides	J. B. Goodenough P. M. Raccah	
1175	Determination of Magnetic Ordering in Heisenberg Magnets from High-Temperature Expansions	T. A. Kaplan H. E. Stanley K. Dwight N. Menyuk	
1176	Magnetic Properties of $MnCr_2S_4$	N. Menyuk K. Dwight A. Wold†	
1177	Diffuse Paramagnetic Neutron Scattering in Chromium Spinels	K. Dwight N. Menyuk T. A. Kaplan	
1242	Band Structure of Gadolinium Metal	J. O. Dimmock A. J. Freeman† R. E. Watson†	

* Division 7.

† Author not at Lincoln Laboratory.

Unpublished Meeting Speeches (Continued)

MS No.			
1192	Pseudo-Binary InSb-InTe System	A. J. Strauss M. D. Banus M. C. Finn	Electrochemical Society, Washington, D. C., 11-15 October 1964
1194	Growth of Sapphire Crystals from the Melt in a Resistance Furnace	T. B. Reed R. E. Fahey	
1191	Reflectivity of Mg_2Ge from 0.5 to 11.0 ev	W. J. Scouler G. B. Wright	American Physical Society, Chicago, Illinois, 23-24 October 1964
1201	Optical deHaas-Shubnikov Effect	J. G. Mavroides M. S. Dresselhaus	
1208	Magnetic Exchange Interactions	J. B. Goodenough	AIME, Philadelphia, Pennsylvania, 19 October 1964
1219	Solid State Plasma Research at Lincoln Laboratory	A. L. McWhorter	Joint Seminar of Plasma Dynamics and Microwaves and Plasmas, M. I. T., 23 October 1964
1223	Experimental Band Structure Studies – Gray Tin and Zinc Blende Mercury Compounds	S. H. Groves	Seminar, M. I. T., 30 October 1964
1230	Far Infrared Studies in Semimetals	D. H. Dickey	Fourth Industrial Liaison Symposium, M. I. T., 19-20 November 1964
1233	Magneto-Optical Phenomena in Solids	J. G. Mavroides	Colloquium, Boston College, 18 November 1964
1243A-D	Recent Advances in Semiconductor Lasers	R. H. Rediker	Seminar, California Institute of Technology, 2 December 1964; Yale University, 9 December 1964; M. I. T., 11 December 1964; Northeastern University, 15 December 1964
1245	Recent Developments in Crystal Growth	T. B. Reed	Materials Science Colloquium, University of Connecticut, 24 November 1964
1246	Effects of Strain on Infrared Absorption Spectra of Sulfur Doped Silicon	W. E. Krag W. H. Kleiner H. J. Zeiger S. Fischler	American Physical Society, Berkeley, California, 21-22 December 1964
General	Complex vs Band Formation in Cubic Bronzes	J. B. Goodenough	Harvard-M. I. T. Joint Physical Chemistry Colloquium, 17 December 1964

I. SOLID STATE DEVICE RESEARCH

A. LONGITUDINAL INJECTION-PLASMA LASER OF InSb

We have obtained coherent emission in n^+pp^+ InSb structures parallel to the direction of the diode current, as illustrated in Fig. I-1. Large-volume luminescence and coherent emission were previously obtained in similar n^+pp^+ InSb structures, but the coherent beam was emitted perpendicular to the direction of current,[1] as in all other existing semiconductor lasers. However, the large active regions of these InSb diodes in which lifetimes of 10^{-7} to 10^{-6} sec permit population inversion in regions of the order of 100 microns away from the injecting contacts are naturally suited for laser oscillations longitudinal to the current, provided a suitable Fabry-Perot cavity can be constructed in that direction and provided lasing in the perpendicular direction is inhibited. Such lasers are free from some of the structural restrictions of the perpendicular lasers. For example, they can be more readily constructed in arrays. They also promise to emit coherently over large areas, and with small beam angles, and they should be suited for large power outputs.

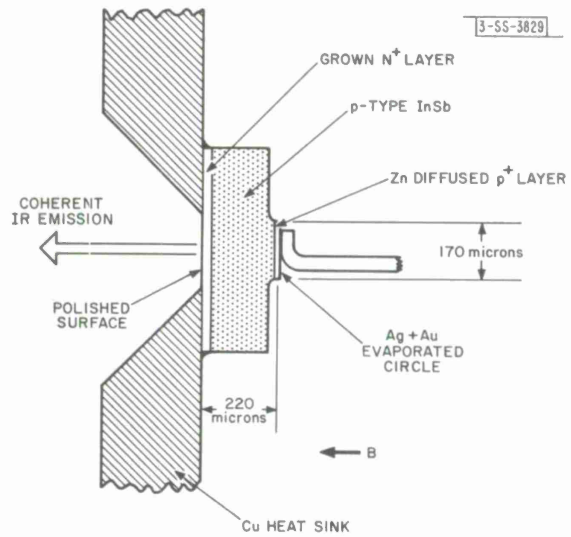

Fig. I-1. InSb n^+pp^+ structure with Fabry-Perot cavity designed for coherent emission parallel to current.

As shown in Fig. I-1, the laser is mounted on a copper heat sink over a small hole. An n^+ layer is grown on a (100) plane of the p-type base ($N_A - N_D \approx 3 \times 10^{13}$ cm^{-3} at 77°K) by a solution-regrowth technique similar to that developed by Nelson[2] for GaAs and germanium. A p^+ layer is formed by zinc diffusion. The laser cavity consists of an optically flat polished surface on the n^+ side and a parallel surface on the p^+ side polished prior to the zinc diffusion. The p^+ surface is made totally reflecting by evaporating layers of silver and gold on a small circle, which also serves as an electrical contact. Contact to the n^+ layer is made by soldering directly to the copper heat sink with an In-Te alloy. To reduce the transverse dimension of the active region, the p^+ layer outside the evaporated circle is removed by etching. In addition, the following factors tend to prevent radial spreading of the plasma, thereby producing an active region

which is long in the direction of the current, extending between the p^+ circle and the high conductivity ($N_D \approx 7 \times 10^{18}$ cm^{-3}) n^+ region. First, the lifetime of electrons inside the plasma is about 10^3 times shorter than outside, which tends to localize the injected carriers as noted earlier in such plasmas.[3] A second collimating effect is due to the external magnetic field which was applied longitudinal to the plasma, as indicated in Fig. I-1. The presence of this magnetic focusing was observed in the voltage-current characteristics of the devices with fields of a few kilogauss. A third factor is the pinch-effect of the azimuthal self-magnetic field in the plasma.[4-6] Pinching of this kind, however, is counteracted by the applied longitudinal magnetic field, and does not appear to be a major factor under conditions existing in these devices, particularly since appreciable pinching would prevent lasing in the "transverse" lasers.[1]

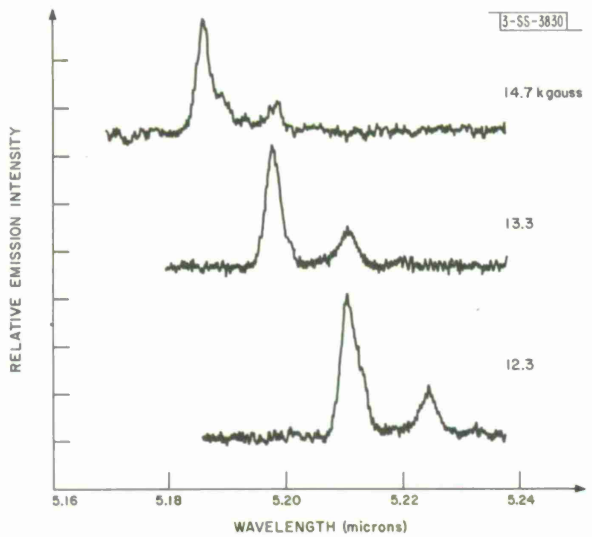

Fig. I-2. Mode structure of longitudinal laser of Fig. I-1 for three values of magnetic field applied parallel to current. Laser was operated near 10°K with 45-amp, 50-nsec pulses.

Coherent emission was obtained near 10°K with 50-nsec current pulses of 20 amp (6×10^4 amp cm^{-2}), with a minimum longitudinal magnetic field of 7 kgauss. Figure I-2 shows the mode structure for three values of magnetic field. Comparison of the wavelength and the magnetic shift with earlier data on InSb diodes[7,8] indicates that the highest energy state of the spin-split lowest Landau level is involved in the transition. The mode spacing near 13 kgauss is 120 Å and remains very nearly at this value as the wavelength is shifted over 1300 Å by a magnetic field change of 11.3 kgauss. As in earlier experiments,[9] the mode position changed slightly with magnetic field due to a change in the index of refraction. For the longitudinal cavity length of 220 microns, the experimental mode spacing corresponds to a value of 5.2 for $[n_o - \lambda_o(dn/d\lambda)]$. The good agreement of this value with values for $[n_o - \lambda_o(dn/d\lambda)]$ obtained in transverse InSb lasers allows us to conclude that oscillations indeed occur in the longitudinal cavity.

I. Melngailis

B. PROPERTIES OF PbSe DIODE LASER

1. Introduction

Semiconductor diode lasers are characterized by population inversion caused by minority carrier injection across a forward biased p-n junction. Diode laser action was first obtained in

GaAs and subsequently in other III-V compounds and alloys. These developments are reviewed in, for example, Ref. 10. Observation of diode laser action in PbTe (Ref. 11) broadened the scope of laser materials to include the lead salts, and in this Solid State Research Report we discuss the next addition to the field, the PbSe diode laser.[12] Laser action in PbSe occurs at 8.5 microns and extends the long wavelength limit for infrared diode lasers beyond the previous value of 6.5 microns set by PbTe.

It is significant that the PbSe laser line occurs in the 8- to 14-micron atmospheric window. Attenuation of infrared radiation due to scattering in most types of haze resulting from dust, soot, smoke, etc. (excluding water droplets) varies as λ^{-4} over the portion of the spectrum covered by diode lasers.[13] Thus, the PbSe laser at 8.5 microns may ultimately be more suitable for applications involving transmission through the atmosphere than the GaAs laser at less than one micron. Since the magnitude of the energy gap in PbSe is strongly affected by temperature,[14] magnetic field,[15] and pressure[16] the laser can be tuned over a significant range.

Since PbSe is new to the modern field of single-crystal devices and since many of the fabrication techniques for the PbSe diode lasers differ markedly from those used for the III-V diode lasers, the properties of PbSe and the details of laser fabrication will be extensively discussed. Results of spectral measurements for diode currents above and below the threshold for laser action are presented and preliminary results on the shift in the spectral position with magnetic field are described.

2. Properties of PbSe

PbSe possesses a rock salt crystal structure, unlike the more familiar III-V compounds, which have the zinc-blende structure. PbSe is able to exist as a stable compound under fairly wide deviations from the stoichiometric composition of equal numbers of lead and selenium atoms. Furthermore, since every excess lead atom in the lattice gives rise to an electron donor and every excess selenium atom to an acceptor, the carrier concentration and type can be controlled by adjusting the Pb:Se ratio in a pure crystal. PbSe may be doped n-type to a concentration as high as approximately 5×10^{19} electrons cm^{-3} by the addition of excess lead, or p-type to about 10^{19} holes cm^{-3} by the addition of excess selenium.[17] In our fabrication procedures, carrier type and concentration were controlled in this manner.

Since the conduction band minima and valence band maxima for PbSe both occur on the $\langle 111 \rangle$ axes at the Brillouin zone surface (L-points),[18] it is a direct-gap semiconductor with a four-fold minimum energy gap in k-space. This band structure is in contrast to that for the III-V compounds which possess single minimum energy gaps at the zone center (Γ-point). For PbSe, the surfaces of constant energy near the edges of both bands are prolate spheroids with major axes in the $\langle 111 \rangle$ directions and anisotropy ratios of approximately 2.0. The dependence of energy on k is nonparabolic, hence the effective masses are concentration dependent. The transverse mass at the band edges for both electrons and holes is 0.049 electron mass units.[15]

Carrier mobilities are approximately equal for electrons and holes. In a well-prepared crystal, the mobility may be 10^3 $cm^2 volt^{-1} sec^{-1}$ at room temperature, 3.5×10^4 $cm^2 volt^{-1} sec^{-1}$ at 77°K and 5×10^5 $cm^2 volt^{-1} sec^{-1}$ at 4.2°K.

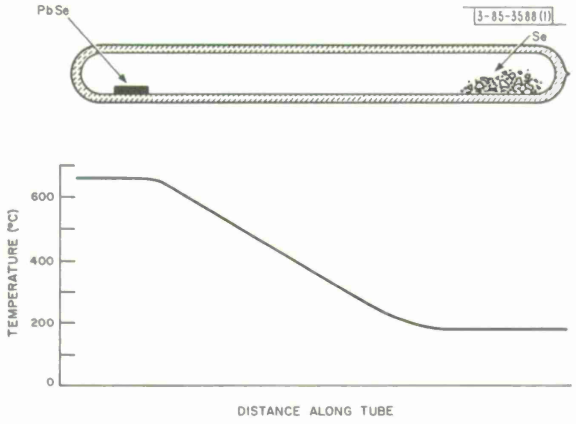

Fig. I-3. Annealing of single crystal PbSe. Temperature profile along sealed quartz tube during annealing is shown. Upper and lower temperatures are 654° and 195°C. A one-week anneal at these temperatures produces n-type PbSe with 3×10^{17} electrons cm^{-3}.

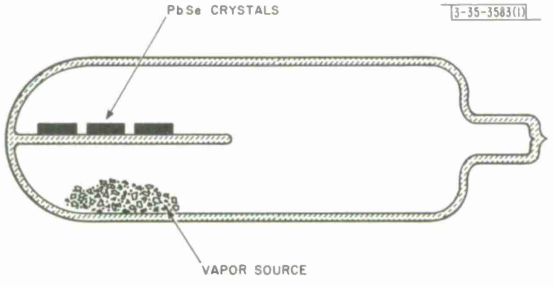

Fig. I-4. Formation of diffused p-n junctions in PbSe. PbSe crystals and a two-phase PbSe, either lead- or selenium-rich, vapor source are in separate sections of a sealed quartz ampoule.

3. Annealing and Fabrication Techniques

The desired carrier type and concentration in PbSe was obtained by an annealing process[19] utilizing the property that for a given crystal temperature, the equilibrium Pb:Se ratio is determined by the selenium vapor pressure which, in turn, is controlled by the temperature of a charge of pure selenium. As shown in Fig. I-1, 2-mm thick wafers of PbSe, which had been previously cut from a Bridgman grown n-type boule having an as-grown electron concentration of about 3×10^{18} cm^{-3}, and a charge of pure selenium were placed at opposite ends of a quartz tube. The tube was evacuated, back-filled with argon to a pressure of 100 torrs and sealed off before being placed in a two-zone furnace with the temperature profile shown in the figure. The parameters given in the caption of Fig. I-3 resulted in an n-type crystal with 3×10^{17} electrons cm^{-3} and a 77°K Hall mobility of 36,000 cm^2 volt^{-1} sec^{-1}. For wafer and selenium temperatures of 659° and 211°C, respectively, a p-type crystal resulted with 5×10^{17} holes cm^{-3} and a Hall mobility of 33,000 cm^2 volt^{-1} sec^{-1} at 77°K. Annealing times were of the order of a week. The high-temperature equilibrium conditions were frozen in by quenching to room temperature. Both n- and p-type annealed PbSe has been used for fabricating diode lasers.

In preparation for forming planar diffused p-n junctions,[20] rectangular parallelepipeds with linear dimensions less than 1 mm were obtained from the annealed wafers by cleaving on {100} planes. The cleaved samples were placed in one section of a quartz ampoule and a vapor source in another section, as shown in Fig. I-4. To form an n-layer on p-type PbSe the vapor source was a lead-rich, two-phase ingot of PbSe; and for a p-layer on n-type material it was a two-phase, selenium-rich ingot, the ingots in both cases being ground to a coarse powder. The loaded ampoule was evacuated, sealed off, heated in a single-zone furnace and quenched in air to room temperature. Diffusion parameters for several concentrations of PbSe are given in Table I-1. It is interesting to note that junctions formed in this manner can be both intrinsic and impurity-free. The techniques of impurity doping used in elemental and III-V semiconductors, on the other hand, produce junction regions that are intrinsic through compensation.

Diodes in the form of rectangular parallelepipeds were formed from the diffused material by further cleaving on {100} planes. Typical dimensions are $0.40 \times 0.18 \times 0.18$ mm, the longer dimension being the distance between the parallel reflecting faces which define the Fabry-Perot structure for laser action. Ohmic contact to p-type PbSe was made with evaporated gold, and to n-type material with indium or an Sn-In alloy. The lasers were mounted in low-inductance, microwave-type packages as shown by the artist's representation in Fig. I-5. Packaging for cryogenic operation is generally not difficult since the thermal expansion coefficients of the lead salts[21] are comparable to those of easily worked metals, such as copper.

It has been found at the Laboratory and by other workers[22] that lead salt crystals may be damaged in the bulk by the sawing, grinding, and polishing techniques that are commonly used with other semiconductors. For this reason, shaping operations in the fabrication of PbSe lasers have been restricted to cleaving, spark-cutting, and etching.

4. Spectral Measurements

The diode lasers were mounted on a conduction-cooled block of a liquid helium dewar equipped with a BaF_2 window. The block temperature was monitored with a GaAs diode thermometer.[23]

TABLE I-1

DIFFUSION PARAMETERS FOR PRODUCING p-n JUNCTIONS IN SINGLE-CRYSTAL PbSe FOR A DIFFUSION TIME OF ONE HOUR. SOURCE INGOT IS TWO-PHASE PbSe WITH Pb:Se ATOMIC PERCENT RATIO OF 51:49 FOR p-TYPE SUBSTRATE AND 49:51 FOR n-TYPE SUBSTRATE.

Crystal No.	Substrate Carrier Type and Concentration (cm^{-3})	Diffusion Temperature (°C)	Junction Depth (cm)
29-63 C-2 (annealed)	$p = 1.5 \times 10^{17}$	350	$< 1 \times 10^{-3}$
29-63 C-2 (annealed)	$p = 1.5 \times 10^{17}$	375	5×10^{-3}
29-63 L-4 (annealed)	$p = 4.7 \times 10^{17}$	530	7×10^{-3}
19733-31 (unannealed)	$p = 1.9 \times 10^{18}$	650	9×10^{-3}
29-63 0-4 (annealed)	$n = 3.1 \times 10^{17}$	450	4×10^{-3}
19733-32 (unannealed)	$n = 4.4 \times 10^{18}$	550	8×10^{-3}

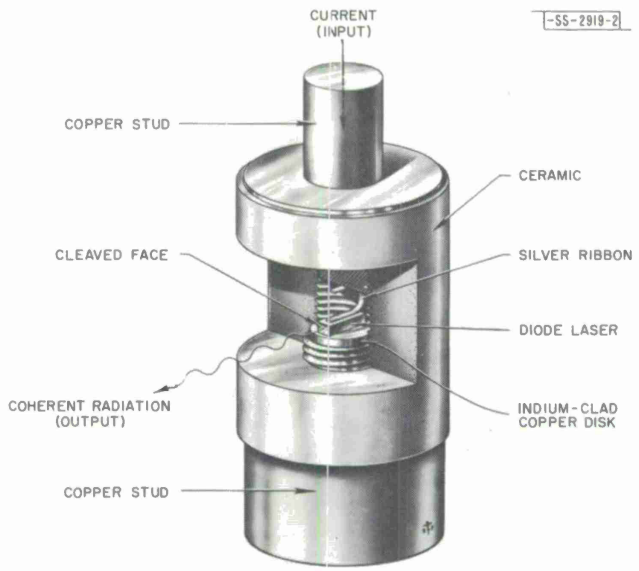

(a)

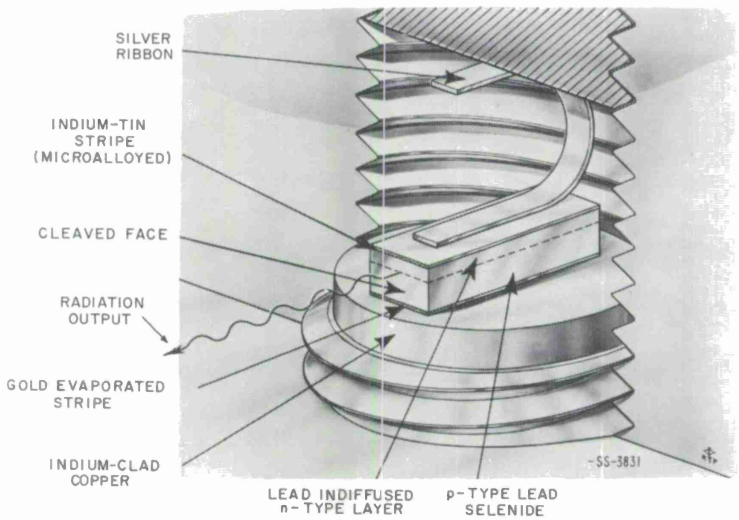

(b)

Fig. I-5. (a) Artist's sketch of low-inductance package for PbSe diode laser: (b) Details of the mounting of a diode laser in its package. Laser shown was fabricated from p-type base material.

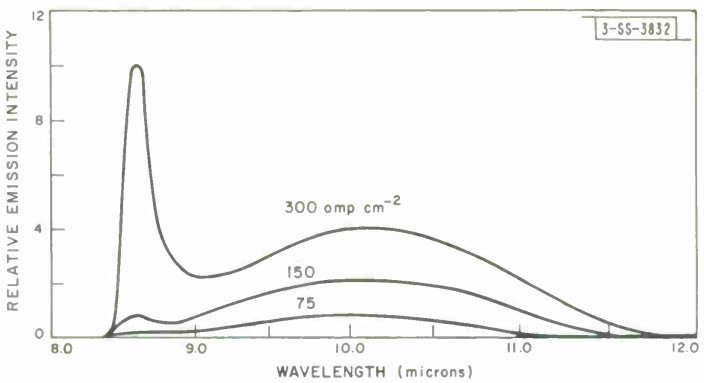

Fig. I-6. Spectra of infrared emission from a PbSe diode laser at 12°K with forward currents below threshold for stimulated emission. Diode area = 10^{-3} cm^2.

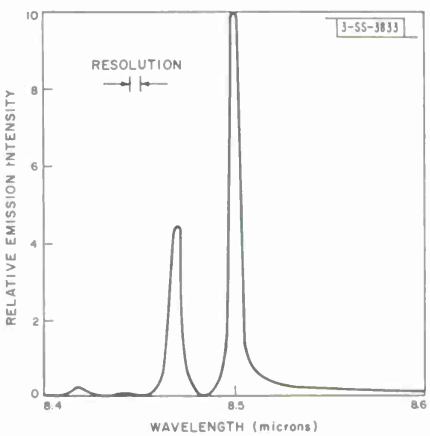

Fig. I-7. Spectrum of coherent infrared emission from a PbSe diode laser at 12°K with forward current well above threshold for stimulated emission. Forward current density = 4,000 amp cm^{-2} and diode area = 2×10^{-4} cm^2.

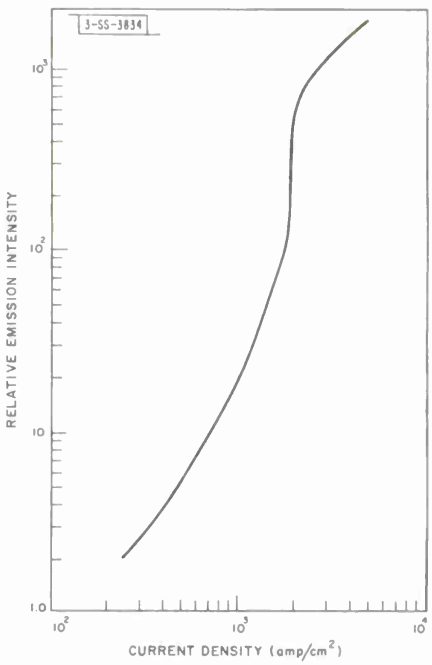

Fig. I-8. Intensity of infrared emission from cleaved end of a PbSe diode laser at 12°K as a function of diode current. Diode area = 2×10^{-4} cm^2.

Forward current was supplied in pulses with pulse width adjusted to eliminate heating. The infrared output from an end face of the diode was focused with f/4 reflecting optics onto the entrance slit of a single-pass monochrometer. The signal was detected by a copper-activated germanium detector whose output was fed into a lock-in amplifier system.

Figure I-6 shows emission spectra from a PbSe diode at a temperature of approximately 12°K for several values of forward-current density. At low currents, a very broad curve with a peak at 10.1 microns is observed. As the current is increased, a narrower second peak becomes evident at about 8.5 microns and the amplitude of this peak increases superlinearly as the current is raised. This superlinearly increasing spontaneous radiation at 8.5 microns soon dominates the diode emission, and above a threshold current density laser action at this wavelength is observed. The spectrum of coherent radiation from the laser at a current well above threshold is shown in Fig. I-7. The average wavelength separation between the modes in Fig. I-7 is 287 Å. Using the usual expression for the axial mode spacing in the Fabry-Perot cavity of length 0.4 mm, the room-temperature value of 4.8 for the refractive index[24] and neglecting the dispersion term, the mode separation is calculated to be 200 Å, in good agreement with the measured value. The 50-Å width of the main peak shown in Fig. I-7 is resolution limited. The absolute intensity of the coherent radiation in Fig. I-7 is, of course, many orders of magnitude larger than the absolute intensity of the spontaneous radiation in Fig. I-6.

Figure I-8 is a plot of radiation intensity from the end face of a diode as a function of current density. The rapid rise at low currents reflects the superlinear behavior of the 8.5-micron peak with current. The break in the curve at about 2,000 amp cm^{-2} corresponds to the onset of laser action. At higher currents, the slope becomes linear, indicating that the quantum efficiency reaches a limiting value. This behavior of emission with diode current differs from that of the III-V diode lasers for which the spontaneous radiation generally increases linearly with current, and superlinear behavior is usually associated with the onset of laser action.

Preliminary measurements have been made of the effect of a magnetic field on the laser output. With the magnetic field parallel to the diode current, a $\langle 100 \rangle$ crystallographic direction, the peak of the laser emission in which cavity mode structure was not resolved was observed to shift linearly at the rate of 7.1×10^{-8} ev/gauss or 17 Mcps/gauss. Results from interband magneto-absorption studies,[15] predict this magnetic shift for emission associated with band-to-band transitions. The magnetic field also reduced the threshold current density from its zero-field value of 2,000 amp cm^{-2} to 500 amp cm^{-2} at a field of about 10 kgauss. For fields above this value, the threshold increased slowly with increasing field. The initial decrease in threshold appears similar to the effect observed with InSb by Phelan, et al.[25]

5. Conclusions

The PbSe diode laser, with a coherent emission peak at 8.5 microns at 12°K, has been developed. Fabrication techniques are based on controlling carrier type and concentration by adjusting the Pb:Se ratio, rather than by adding impurities. The diode emission below threshold exhibits two spectral peaks, one with a maximum near 8.5 microns which increases superlinearly with current and another with a maximum at 10.1 microns which increases slowly with current. Laser action associated with the 8.5-micron peak occurs above a threshold current density of

2,000 amp cm^{-2}. The unresolved emission peak shifts linearly to higher energies with $\langle 100 \rangle$-oriented magnetic field intensity at the rate of 7.1×10^{-8} ev/gauss, or 17 Mcps/gauss, which is the expected value if the emission is associated with band-to-band transitions. The threshold current density decreases to a fraction of its zero-field value in a magnetic field of approximately 10 kgauss, then rises slowly with increasing field. The PbSe laser should eventually be of particular interest for communications since its emission is in the 8- to 14-micron atmospheric window, a spectral region of high atmospheric transparency where attenuation due to scattering by haze is generally low.

J. F. Butler
A. R. Calawa
R. H. Rediker

REFERENCES

1. I. Melngailis, R. J. Phelan, Jr., and R. H. Rediker, Appl. Phys. Letters 5, 99 (1964).
2. H. Nelson, RCA Review 24, 603 (1963).
3. I. Melngailis and R. H. Rediker, Proc. IRE 50, 2428 (1962).
4. M. Glicksman and M. Steele, Phys. Rev. Letters 2, 461 (1959).
5. M. Glicksman and R. A. Powers, Phys. Rev. 121, 1659 (1961).
6. A. G. Chynoweth and A. A. Murray, Phys. Rev. 123, 515 (1961).
7. R. J. Phelan, Jr., A. R. Calawa, R. H. Rediker, R. J. Keyes, and B. Lax, Appl. Phys. Letters 3, 143 (1963).
8. R. L. Bell and K. T. Rogers, Appl. Phys. Letters 5, 9 (1964).
9. R. J. Phelan, Jr., and R. H. Rediker, Proc. IEEE 52, 91 (1964).
10. G. Burns and M. I. Nathan, Proc. IEEE 52, 770 (1964).
11. J. F. Butler, A. R. Calawa, R. J. Phelan, Jr., T. C. Harman, A. J. Strauss, and R. H. Rediker, Appl. Phys. Letters 5, 75 (1964).
12. J. F. Butler, A. R. Calawa, R. J. Phelan, Jr., A. J. Strauss, and R. H. Rediker, Solid State Commun. 2, 303 (1964).
13. P. W. Kruse, L. D. McGlauchlin, and R. B. McQuistan, Elements of Infrared Technology: Generation, Transmission and Detection (Wiley, New York, 1962), Chap. 5.
14. A. F. Gibson, Proc. Phys. Soc. (London) B65, 378 (1952).
15. D. L. Mitchell, E. D. Palik, and J. N. Zemel, Symposium on Radiative Recombination in Semiconductors, Paris, 27-28 July 1964.
16. A. R. Calawa, J. F. Butler, and R. H. Rediker, Bull. Am. Phys. Soc. 10, 84 (1965).
17. R. F. Brebrick and E. Gubner, J. Chem. Phys. 36, 170 (1962).
18. M. R. Ellet and K. F. Cuff, Bull. Am. Phys. Soc. 8, 601 (1963).
19. K. Igaki and N. Ohashi, J. Phys. Soc. Japan 18, 143 (1962).
20. J. F. Butler, J. Electrochem. Soc. 111, 1150 (1964).
21. S. I. Novikova and N. Kh. Abrikosov, Sov. Phys. – Solid State 5, 1397 (1964).
22. Y. Sato, M. Fujimoto, and A. Kobayashi, Jap. J. Appl. Phys. 2, 688 (1963).
23. B. G. Cohen, W. B. Snow, and A. R. Tretola, Rev. Sci. Instr. 34, 1091 (1963).
24. A. K. Walton and T. S. Moss, Proc. Phys. Soc. 8, 601 (1963).
25. R. J. Phelan, Jr., A. R. Calawa, R. H. Rediker, R. J. Keyes, and B. Lax, Appl. Phys. Letters 3, 143 (1963).

II. LASER RESEARCH

A. RAMAN LASER PROGRAM

1. Stimulated Brillouin Emission at 90° to Ruby Beam

Stimulated Brillouin laser action in nitrobenzene has been observed at 90° to the ruby beam using the same physical arrangement as was used for the 90° stimulated Raman experiment described previously.[1] Slight changes were made to isolate the effects from one another.

If the mirrors used in the 90° cavity reflect at 6940 as well as 7650 Å, then both effects are observed simultaneously, and in fact, S_1 Brillouin and S_1, S_2, and S_3 Raman emission have been observed on the same 1Z infrared plate. However, if mirrors are used that reflect 6940 but not 7650 Å, the Raman emission is not observed. This enables a study of the Brillouin emission without fogging the infrared film with Raman radiation. Conversely, if the mirrors reflect 7650 and not 6940 Å, then the Brillouin emission is not present.

Study with an external etalon crossed with a prism shows that the Brillouin emission is about 0.03 cm^{-1} or 1 kMcps wide, whereas the Raman emission extends over 1.5 to 3 cm^{-1}. There is some evidence in these pictures of quenching of the Brillouin effect by a strong Raman effect.

The 90° nonstimulated Brillouin shift in nitrobenzene was measured with a He-Ne laser by the same method used by Chiao and Stoicheff.[2] The shift was 5 kMcps, as shown in Fig. II-1. The 180° shift calculated from this is 7.1 kMcps. This number agrees closely with that obtained in 180° stimulated Brillouin emission with ruby by Garmire.[3]

External etalon photographs of the 90° stimulated Brillouin output (Fig. II-2) show one Brillouin mode designated B_1 and sometimes another ring, designated B_2, between 6.8 and 7.1 kMcps away from B_1. None of the primary ruby radiation appears in Figs. II-1 and II-2.

In order to see the relationship between the ruby modes and the first Brillouin (B_1) ring, some of the 0° ruby energy was fed around by a mirror and added to the 90° emission analyzed by the external etalon. A typical picture is shown in Fig. II-3. A study of many of these pictures shows that, in general, no one ruby mode is exactly 5 kMcps away from the first Brillouin ring. Therefore, one of the ruby modes alone could not have produced the B_1 ring by itself.

Each ruby mode produces a Lorentzian-shaped gain line spaced 5 kMcps from itself. The composite gain line is a sum of these, and its shape depends on the relation between the spacing of the ruby modes and the bandwidth of the Brillouin scattering process. An upper limit to the width of the process is known from the fact that the nonstimulated emission is no wider than the 0.6-kMcps gas laser that produced it. The width of a single ruby mode is also approximately 0.6 kMcps so, in this case, the Lorentzian gain line will be of this width, and the composite line will have peaks which are double the amplitude of the valleys.

A study of many far-field patterns indicates that the system usually, but not always, oscillates in an on-axis mode of the cavity with radiation extending about 1 kMcps around the center frequency. Hence, the resonant cavity of 4.7-kMcps interorder spacing usually picks a frequency on the composite gain line at which to oscillate, which is not always a peak of the line.

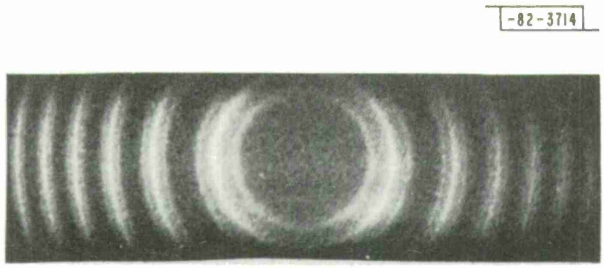

Fig. II-1. 90° incoherent Brillouin scatter using a 13-mw 6328 Å He-Ne laser source. Etalon spacing is 0.25 inch. Center ring of each group is laser light. Outer ring is anti-Stokes, inner ring is Stokes scatter. Magnitude of the shift is 5 kMcps.

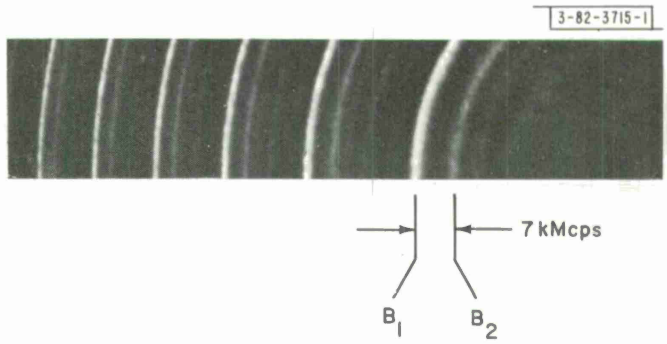

Fig. II-2. External etalon analysis of 90° Brillouin output. Etalon spacing is 0.25 inch.

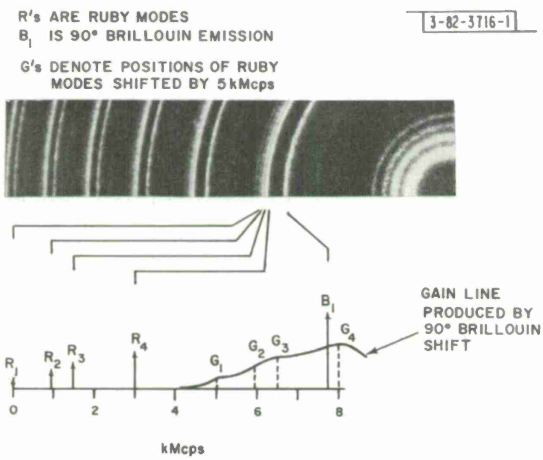

Fig. II-3. Relationship of ruby frequency modes to 90° Brillouin output.

Occasionally, the far-field pattern is dark in the center indicating off-axis oscillation in the main B_1 line.

Bloembergen and Shen[4] have shown that different ruby pump modes couple to each other through the Raman effect and produce cross terms in the Raman gain expression that result in more gain than if the same energy were put into a single ruby mode. This same argument, applied to the Brillouin case, might explain the difficulty in doing the 90° Brillouin experiment with a single-frequency ruby pump. Threshold was never reached with a single mode of 0.2 Mw using a passive Q-switched ruby. It is estimated that the rotating mirror system gives about 0.5 Mw in its stronger modes so that it is impossible to rule out that more power in a single mode might reach threshold. All attempts to produce a single mode from the rotating mirror system failed.

This experimental configuration enables the gain of the Brillouin scattering medium to be measured from the conditions at threshold. Reamplification of the scattered light in the ruby, which occurs in the 180° backscattered experiments, does not occur in this 90° configuration. The threshold for this stimulated Brillouin effect is about 3 Mw from our $\frac{1}{4}$-inch rod. The rod is judged to be lasing strongly over 5 mm of its diameter. This is the "path length" for gain across the cylindrical focus. The cylindrical lens concentrates the beam 10:1 in one dimension giving an active area of 0.05 cm^2. The gain at threshold is estimated to be

$$\alpha = \frac{1-R}{\ell} = \frac{1-0.991}{0.5\ \text{cm}} = 0.02\ \text{cm}^{-1} \text{ at } 60\ \text{Mw/cm}^2 \text{ incident flux} \quad .$$

At 5-Mw ruby power, or 100-Mw/cm^2 power density, the 90° Brillouin output is estimated to be 1 kw. Inside the cavity of 99.1-percent mirrors, the power is then about 100 kw. The threshold for this 90° experiment is somewhat lower than that reported for the 0° experiment using a spherical focus, but no resonator[3] around the active medium.

There is reason to wonder how a 100-kw (inside the cavity) B_1 line can produce a B_2 line by the process of 180° Brillouin scattering when the threshold for the production of the B_1 line is 3 Mw or an average of about $\frac{1}{2}$ Mw per (strong) mode of the ruby. One possible explanation is that the threshold for a 180° backward wave process is lower than for the 90° process, or that there is some additional gain from additional ruby modes spaced 5 kMcps above the B_2 line. The B_2 line is shown in Figs. II-2 and II-4.

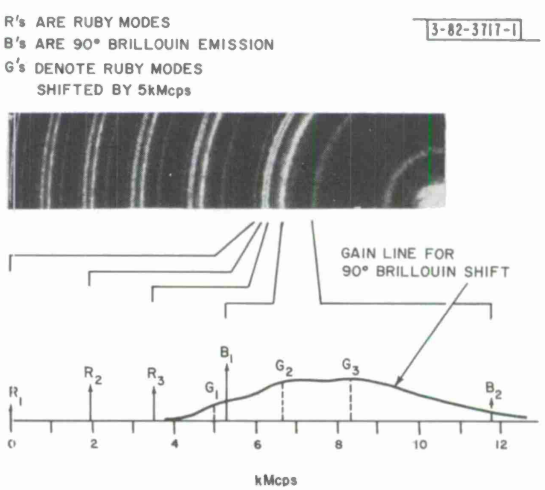

Fig. II-4. External etalon analysis of sum of 90° Brillouin output and a small amount of ruby pump light in a case when a second Brillouin line B_2 is present.

The ability of the cavity of 4.7-kMcps interorder spacing to support two modes, B_1 and B_2, 7 kMcps apart, can be explained by the fact that a plane parallel cavity with an aperture as large as its spacing can have walkoff modes of considerable angle. If the B_1 mode is assumed to oscillate on the axis of the cavity, there will be well over 100 passes before the B_2 mode, which is $7.0 - 4.7 = 2.3$ kMcps from an on-axis resonance, walks off the mirrors of 2-cm aperture.

The stimulated Brillouin effect might be even better for multiple pumping schemes[5,1] to obtain high power, with high spatial mode purity than is the Raman effect. The phonon created is of much lower energy and hence results in much less local heating of the medium to cause index of refraction changes and a degradation of optical quality.

2. Stimulated Raman Emission at 90° to Ruby Beam

Some additional work has been done on the 90° Raman experiment. The 90° Raman output in nitrobenzene was analyzed with an external etalon, and no structure was observed in the rings. The output was a continuum of about 2-cm^{-1} width. It was conjectured that the plane parallel Raman cavity was oscillating in walkoff modes which could then range in frequency continuously around the center frequency.

To show this, the far field pattern of the 90° Raman output was focused in a plane. Then, a slit was used to block off most of the off-axis energy. The remaining energy, when fed into an etalon, showed a large number of modes separated by the interorder spacing of the Raman cavity covering a range of approximately 2 cm^{-1}.

Jane H. Dennis

3. Stimulated Stokes and Anti-Stokes Radiation from a Point Source

We have considered a model for the Stokes and anti-Stokes radiation arising from a point source at the Stokes frequency in a Raman-active medium. The coupled Fourier transform equations for the Stokes and anti-Stokes fields are used to obtain an exact Fourier integral expression for the Stokes and anti-Stokes fields. These Fourier integral expressions are evaluated asymptotically using a saddle-point method. It is found that, to lowest order in the Raman gain and coupling constants, the Stokes wave grows in a spherical wave from the point source with the same growth constant in the phase-matched direction as in other directions. The reaction of the anti-Stokes radiation on the Stokes radiation in the phase-matched direction produces only a relative suppression in higher order; the growth, however, remains exponential.

The anti-Stokes radiating wave in the Raman-active medium is exponentially damped, because the source of phase-matched anti-Stokes radiation is a narrow cone of polarization at the anti-Stokes frequency associated with the phase-matched Stokes radiation, and as the anti-Stokes radiation propagates away from this active cone, it is damped by the anti-Stokes damping of the active medium. Thus, the only anti-Stokes radiation observed externally is the radiation produced by the polarization at the anti-Stokes frequency within the phase-matched Stokes cone and a boundary of the Raman-active medium.

H. A. Haus*
P. L. Kelley
H. J. Zeiger

* Department of Electrical Engineering, M.I.T.

B. CW TWO-PHOTON PHOTOELECTRIC EFFECT

We have observed continuous double-photon photoelectric emission from Cs_3Sb using the 1.153-micron radiation from a He-Ne gas laser. The first observation of this effect[6] utilized a pulsed solid-state laser. In our experiment, the laser light was focused upon the cathode of an RCA 1P21 photomultiplier tube by a 4.8-cm focal-length lens. With the laser output set at 1.35 mw, calibrated attenuators were employed to vary the power incident upon the cathode surface. Reflection losses between the exit mirror of the laser and the cathode amounted to 30 percent.

Figure II-5 shows preliminary results obtained with the laser oscillating in a higher-order mode whose pattern occupied an area approximately 5 mm in diameter at the plane of the lens. In computing the current and power densities of Fig. II-5 it was assumed that the focal spot had an area of 10^{-5} cm^2, which is approximately five times the theoretical diffraction-limited focal spot area of the TEM_{ooq} mode. Unfortunately, the focal spot was small enough to reveal nonuniformities across the cathode surface, thus hampering reproducibility of the data. Also, a fraction of the convergent laser beam was intercepted and scattered by the grill wires used for electrostatic focusing of the emitted electrons.

The quadratic portion of the curve in Fig. II-5 represents two-photon-induced emission as discussed by Sonnenberg, et al.[6] The linear portion is characteristic of a one-photon process, and similar behavior has been seen by Teich, et al.,[7] in a two-photon experiment with sodium metal. In the present experiment, the linear portion may be attributed to the finite occupancy of the conduction band of Cs_3Sb and to the presence of occupied impurity levels and other states in the forbidden band lying within about 0.7 ev of the bottom of the conduction band.

R. A. Soref

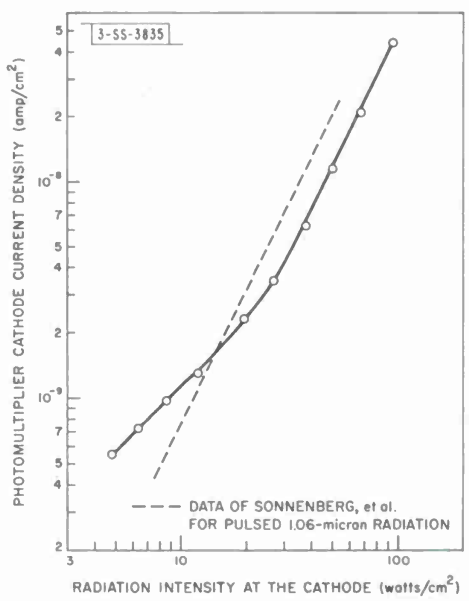

Fig. II-5. Photoemissive response of Cs_3Sb cathode to CW 1.153-micron radiation.

-SS-3836

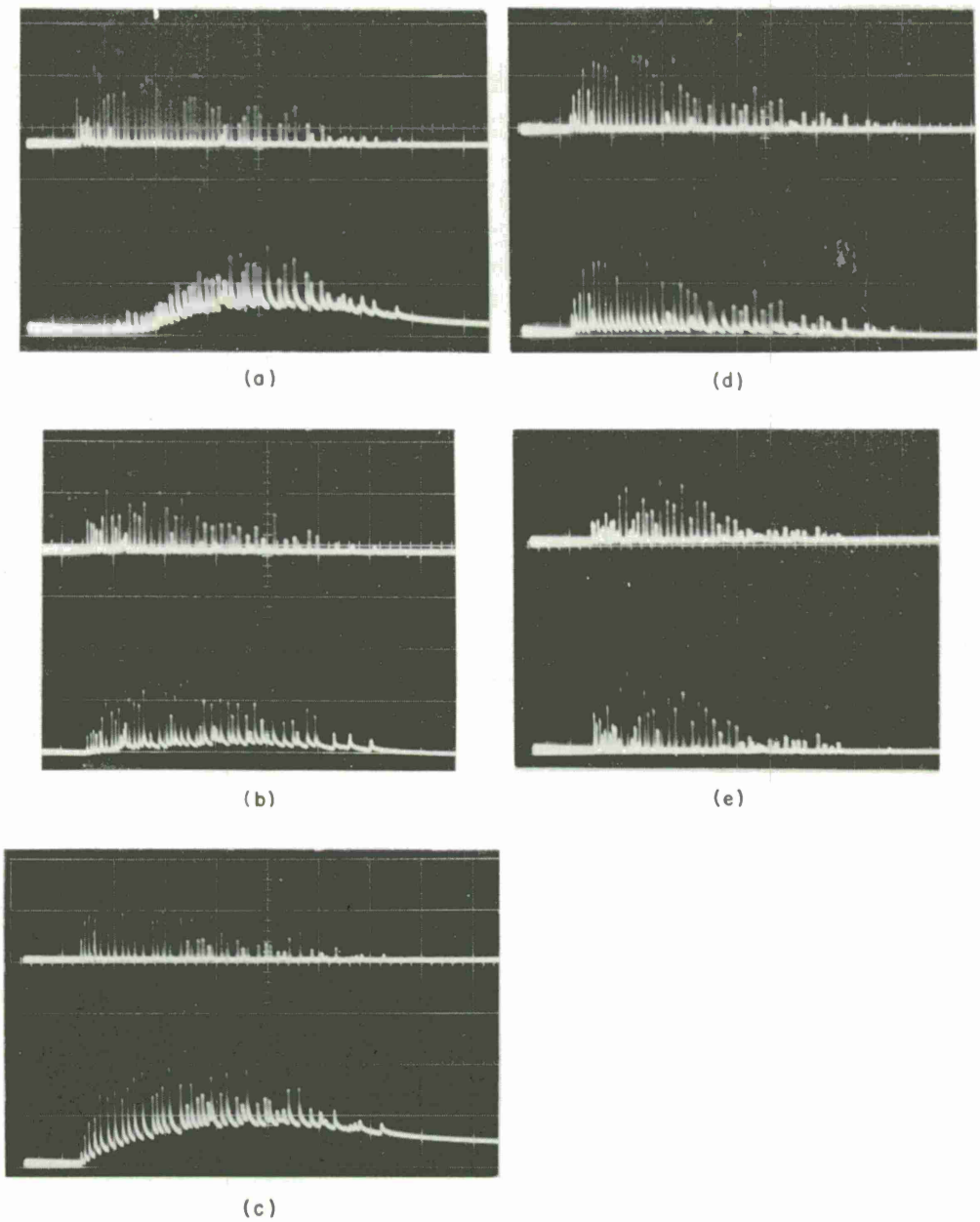

Fig. 11-6. Photoconductive response of semiconductor samples to unfocused 6943-Å laser radiation: (a) High-purity CdS, $\rho_o = 5 \times 10^9$ ohm-cm; (b) CdS, $\rho_o = 3 \times 10^3$ ohm-cm; (c) CdS, $\rho_o = 5$ ohm-cm; (d) High-purity ZnS, $\rho_o = 3 \times 10^{11}$ ohm-cm; (e) High-purity ZnSe polycrystal, $\rho_o = 2 \times 10^{10}$ ohm-cm. Upper trace: laser intensity. Lower trace: photocurrent, time scale = 50-μsec div^{-1}.

C. TWO-PHOTON PHOTOCONDUCTIVITY

If a semiconductor is illuminated with intense optical radiation of frequency ω, double-photon absorption will occur provided $\omega < h^{-1}E_g < 2\omega$, and the hole-electron pairs thereby created will alter the electrical conductivity of the crystal. We have attempted to observe "second-order" photoconduction of this sort in monocrystals of CdS, ZnS, and ZnSe using ruby laser radiation. Representative preliminary results are shown in Fig. II-6. The largest laser spikes in Fig. II-6 correspond to a peak flux of about 10^{22} photons cm^{-2} sec^{-1} incident upon the samples. Trapping effects may have caused the steady DC rise in photocurrent over a 200-μsec interval in samples (a) and (b), although this behavior is not fully understood at present. Dielectric relaxation may be ruled out on the basis of the low resistivity of sample (b).

As the output energy of the laser was increased from 0.1 to 0.5 joule per flash, it was found that the time-integrated photocurrent of sample (a) increased as the cube of the time-integrated laser intensity, whereas, for samples (d) and (e), the integrated photocurrent increased linearly with the integrated laser intensity. The cubic response has not yet been explained. The linear response could be attributed to two-photon absorption, provided that bimolecular recombination across the gap is the dominant recombination mechanism. However, single-photon impurity absorption can also yield a linear response if a linear recombination process dominates. Therefore, additional data are required to decide how many charge carriers (if any) were produced via two-photon absorption.

R. A. Soref
M. M. Litvak

D. GAS LASER PROGRAM

1. Measurement of Amplitude Noise in Optical Cavity Masers

We report here measurements on the amplitude noise of a cavity-type gaseous optical maser oscillator operating at 6328 Å above and below threshold. We compare our results above threshold with the theory of noise in van der Pol oscillators,[8] which is the proper one to use for the maser oscillator,[9] and the measurement below threshold with the linear theory of maser amplifiers.[10] Because of the quantitative agreement we conclude that the noise is due to spontaneous emission.

We use the equivalent circuit of Fig. II-7. The conductance $G = \omega_o C/Q$ represents the resonator loading by the outside space.

$$G_m = G_m^o (1 - aV^2) = \omega_o C/Q_m$$

is the (usually negative) conductance of the maser material. Above threshold, the magnitude of the negative conductance G_m decreases quadratically with voltage. The uniform spectral density

$$\overline{i^2}/\Delta\nu = 4G_m h\nu (n_2/g_2)/[(n_1/g_1) - (n_2/g_2)]$$

of the noise current generator is chosen so that the power emitted by the cavity below threshold satisfies the well-known linear theory[10] (n_1 and n_2 are the populations of the lower and upper levels, and g_1 and g_2 are their degeneracies). Above threshold, the dependence of the noise

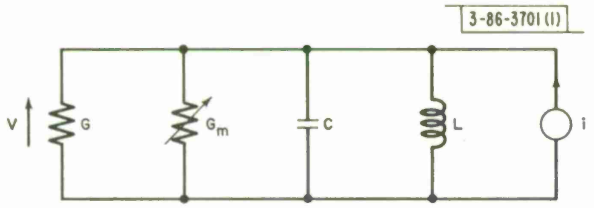

Fig. II-7. Equivalent circuit of van der Pol oscillator with noise.

power upon the population inversion is assumed to be the same as that below threshold. Using the noise power predicted from the equivalent circuit, and the photoemission theory of Kelley and Kleiner,[11] one obtains for the spectrum of the anode current in a photomultiplier illuminated by the maser, operating in a single mode near threshold, both above and below,

$$S(\nu) = 2Ae\Gamma I_a + 4AeI_a\eta\alpha \left(\frac{\Delta\nu_o}{\Delta\nu}\right)^2 \frac{1}{1 + (\frac{\nu}{\Delta\nu})^2} \equiv S_s + S_e \quad . \tag{1}$$

In Eq. (1), A is the photomultiplier gain, e is the electron charge, I_a is the photomultiplier anode current, Γ is the shot-noise enhancement factor caused by secondary emission, η is a loss factor including the quantum efficiency and all other losses between the maser output and photomultiplier, $\alpha = (n_2/g_2)/[(n_2/g_2) - (n_1/g_1)]$, and

$$\Delta\nu = \nu_o \left|\frac{1}{Q} + \frac{1}{Q_m^o}\right| \tag{2}$$

with ν_o, the frequency of the mode. Note, however, that below threshold contributions of other modes than the most strongly excited axial mode become more important as the excitation is decreased; S_s and S_e denote the shot-noise and excess noise, respectively.

The rate $\bar{n}$ of photon emission from the maser above threshold gives information on the coefficient of the nonlinear part of the conductance

$$\bar{n} = \frac{(G_m^o + G)\, G}{2aG_m^o\, h\nu} \quad . \tag{3}$$

Below threshold, one finds

$$\bar{n} = \alpha \frac{2\pi(\Delta\nu_o)^2 \frac{Q}{|Q_m^o|}}{\Delta\nu} \quad . \tag{4}$$

In the experiments, an internal mirror laser of near hemispherical geometry, with a mirror spacing of 50 cm, was used. The inside diameter of the quartz tube was 3.5 mm. The maser was DC-excited (gas discharge fluctuations[12] were suppressed by optimized external circuitry and a magnet near the discharge), and was stabilized to less than 1 percent long-term drift in intensity by a feedback circuit with a time constant of 1/50 sec, by using the light from one of the maser mirrors. The light through the other mirror was fed partly to one photomultiplier connected to a counter, and partly to another connected to a spectrum analyzer. The spectrum was studied in the 0- to 17-Mcps range Different spectrum analyzers were used for the ranges of the frequency

spectrum. Variation in the scanning velocities was from 0 to 4 cps/sec at the low-frequency end to 0 to 1000 cps/sec in the high-frequency range of the spectrum. The corresponding IF bandwidths ranged from a minimum of 10 cps to a maximum of 10,000 cps. The spectrum analyzer output was fed into a spectral density analyzer with integration times of 1 or 5 sec, and then to a chart recorder.

The composite experimental results are shown in Fig. II-8(a-b). The curves are labeled by their corresponding photoelectron rate $\overline{N}$ (in sec^{-1}) at the photocathode. Above threshold, 7 of the 12 dynodes of the photomultiplier were shorted to the anode. Lorentzian curves can be fitted with very good accuracy onto the curves above threshold and to the top curves below threshold. The two curves with the highest ratios S_e/S_s and with the narrowest bandwidths represented the highest power below threshold and the lowest power above threshold at which our maser could operate, stably and reproducibly, for several months. The small spike modulation at approximately 168 kcps, both above and below threshold, is due to residual gas plasma oscillation.

The experimentally observed spectral curves of the photomultiplier current, predicted quantitatively by Eq. (1) and (2), show:

(a) The ratio S_e/S_s (near zero frequency), is proportional to the maser power P below threshold, and inversely proportional to P above threshold. Deviation from the $1/P$ dependence occurs only farther below threshold when more than one linearly polarized mode contributes to the output.

(b) The bandwidth of the excess noise is inversely proportional to P below threshold and directly proportional to P above threshold.

(c) The measured ratio S_e/S_s from the $\overline{N} = 3.68 \times 10^9$ curve above threshold, yields (Ref. 13) $\alpha = 1.97$, using Eq. (1), the measured values of $\eta = 4.9 \times 10^{-3}$, $\Gamma = 1.3$, and taking $\Delta\nu_o = 4.7 \times 10^5$ cps as computed from the transmittance of the mirrors.

(d) From Eq. (1), the ratio S_e/S_s above and below threshold is the same for curves of equal bandwidth if, below threshold, one linearly polarized mode predominates (as is the case in the operating condition of the $\overline{N} = 1.64 \times 10^7$ curve). Note that G_m^o is changed only by a fraction of a percent as the laser is brought from below threshold operation (the $\overline{N} = 1.64 \times 10^7$ curve) to oscillating condition (the $\overline{N} = 3.68 \times 10^9$ curve), and therefore α should not change perceptibly. The two top curves in Fig. II-8(a-b) have comparable bandwidths. If one predicts from the above-threshold curves the ratio S_e/S_s below threshold, taking into account the difference in bandwidths, one finds $S_e/S_s = 4600$ which should be compared with the measured value of 4400 for the case of $\overline{N} = 1.64 \times 10^7$.

(e) From Eq. (4), one may predict the photon emission rate from the maser (with $\alpha = 1.97$ for the curve $\overline{N} = 1.64 \times 10^7$) to be $\overline{n} = 3.22 \times 10^9\ sec^{-1}$. The measured rate was $\overline{N}/\eta = \overline{n} = 3.34 \times 10^9\ sec^{-1}$.

Our measurements of S_e/S_s, bandwidth, and power agree with the theoretically predicted values within 5 to 10 percent which is about the accuracy of our absolute power measurements and the gain stability of photomultipliers in a normal laboratory environment.

We acknowledge many helpful discussions with M. M. Litvak, A. Javan, and A. Szöke.

C. Freed
H. A. Haus

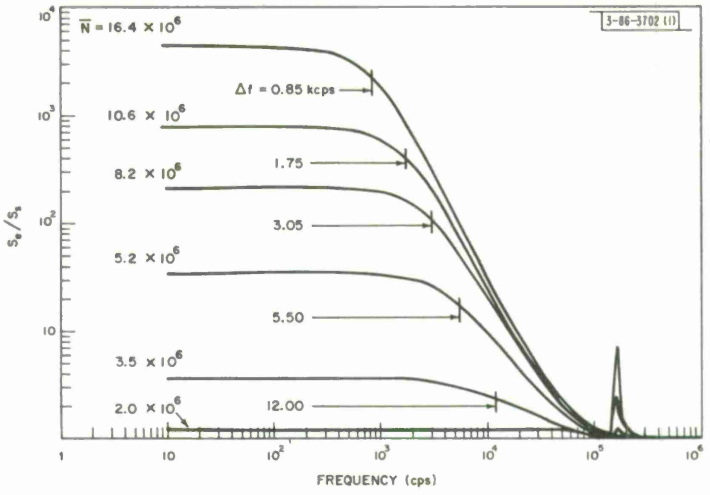

(a) Below threshold operation.

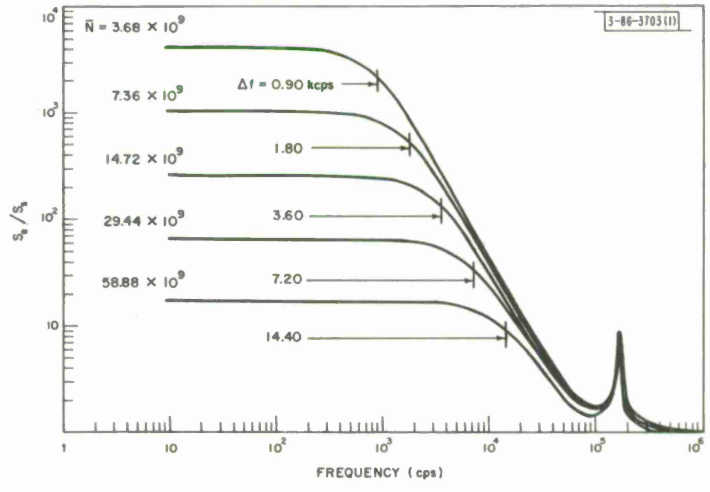

(b) Above threshold operation.

Fig. II-8. Observed photomultiplier current spectra.

2. High-Pressure Mercury Laser

The possibility of a high-pressure mercury arc as a laser medium has been discussed in the last Solid State Research Report.* Since then, it has been shown that the impurity content in a discharge can be controlled well enough so that the mercury molecule upper laser state can be pumped to an appreciable density. Stabilization of the pulsed arc, i.e., keeping the constricted arc straight and parallel to the tube axis, was accomplished by maintaining a milliampere DC discharge through the tube. This worked in a mixture of argon and mercury up to approximately 100 torrs of mercury and 400-amp pulsed current, at which point the arc again became unstable. The upper level population, according to the spontaneous emission, had a greater than linear growth with pressure and arc current up to the unstable region as shown in Fig. II-9.

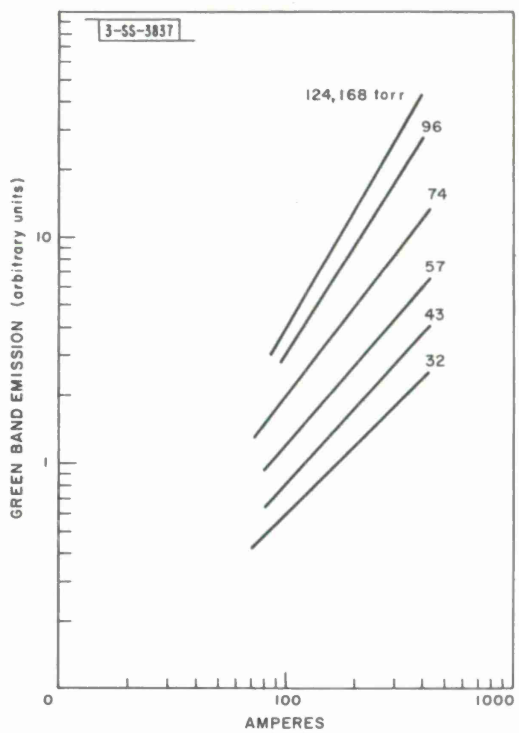

Fig. II-9. Power output in mercury vapor green band as a function of pulsed arc current for specified mercury partial pressures. Argon partial pressure was 25 torrs.

Estimates of the gain from spontaneous emission from the laser state for presently achievable pressure and current conditions indicate that more than 0.3-percent loss in the optical cavity will not allow oscillation. Therefore, an optical cavity is being constructed with mirrors having less than 0.2 percent estimated loss and with a laser tube having Brewster angle windows of less than 0.05-percent loss. Special cleaning and assembly techniques are being used to maintain high quality for operation at about 250°C.

R. J. Carbone
M. M. Litvak

*Solid State Research Report, Lincoln Laboratory, M.I.T. (1964:3).

REFERENCES

1. Solid State Research Report, Lincoln Laboratory, M. I. T. (1964:2), DDC 606126; (1964:3); Jane H. Dennis and P. E. Tannenwald, Appl. Phys. Letters 5, 58 (1964).
2. R. Y. Chiao and B. P. Stoicheff, J. Optical Soc. Am. 54, 1286 (1964).
3. E. Garmire and C. H. Townes, Appl. Phys. Letters 5, 84 (1964); and private communication.
4. N. Bloembergen and Y. R. Shen, Phys. Rev. Letters 13, 720 (1964).
5. W. H. Culver and E. J. Seppi, J. Appl. Phys. 35, 3421 (1964).
6. H. Sonnenberg, H. Heffner, and W. Spicer, Appl. Phys. Letters 5, 95 (1964).
7. M. C. Teich, J. M. Schroeer, and G. J. Wolga, Phys. Rev. Letters 13, 611 (1964).
8. J. A. Mullen, Proc. IRE 48, 1467 (1960); note a factor 1/2 error from Eq. (30) on.
9. W. E. Lamb, Phys. Rev. 134, 6A (1964).
10. M. W. Mueller, Phys. Rev. 106, 8 (1957).
11. P. L. Kelley and W. H. Kleiner, Phys. Rev. 136, A316 (1964).
12. J. A. Bellisio, C. Freed, and H. A. Haus, Appl. Phys. Letters 4, 5 (1964).
13. L. J. Prescott and A. Van der Ziel, Physics Letters 12, 317 (1964); the authors have shown two curves of excess noise above the threshold of oscillation. By comparing the measurements with a linear theory they found values of α that were too small.

III. MATERIALS RESEARCH

A. CZOCHRALSKI GROWTH OF SAPPHIRE CRYSTALS IN A RESISTANCE FURNACE

Because of its high melting point (2050°C) and corrosiveness toward many crucible materials, sapphire (Al_2O_3) has classically been grown by the Verneuil flame fusion technique. Growth of ruby (Cr-doped Al_2O_3) crystals by the Czochralski method has recently been reported by Paladino and Roiter,[1] who used an induction-heated tungsten crucible in a nitrogen atmosphere, and by the Linde Company,[2] which has not described the details of its procedure. We have grown sapphire crystals in a resistance furnace[3] recently developed for operation in oxidizing, neutral, or reducing atmospheres at temperatures up to 2400°C. Sapphire was selected as a trial material in order to test the high-temperature capability of the furnace. The furnace was modified for Czochralski growth by adding mechanisms for raising and lowering the seed and for rotating the seed at 0 to 200 rpm. Sight ports were placed in the furnace lid to allow projection of the image of the melt surface on a screen for monitoring growth. The melt was contained in an iridium or molybdenum crucible under an argon atmosphere. Since the molten sapphire did not evaporate appreciably, it was possible to remove the zirconia tube used to protect the tantalum heater from oxygen and other reactive gases.

A spoke-like pattern of light and dark on the surface of the melt is observed on the monitor screen before the seed is dipped. This pattern is probably caused by convection cells resulting from high temperature gradients in the melt. The existence of such gradients is established by optical pyrometer measurements which show that the temperature of the crucible wall during growth is about 150°C above the melting point of sapphire. After the rotating seed is dipped into the melt, the radial arms of the spoke-like pattern become skewed due to the influence of the seed rotation on the melt. The pattern provides a good view of the growing meniscus. In general, crystal growth starts easily but becomes more difficult to maintain as the crystal becomes longer, probably because the temperature gradient in the solid is not sufficient to stabilize the growing interface.

Crystals grown from iridium crucibles are water-white. Two of these crystals are shown in Fig. III-1. Crystals grown from molybdenum crucibles have a light-gray tinge. This coloration is probably not due to the presence of molybdenum as an impurity, since no molybdenum was detected in a mass spectrographic analysis with a detection limit of 40 ppm. Possibly the coloration is due to an oxygen deficiency resulting from reduction by the molybdenum, which has a greater reducing power than iridium.

T. B. Reed
R. E. Fahey

B. FORCED CONVECTION GROWTH OF IODINE CRYSTALS

The results of initial experiments on the vapor growth of iodine crystals by forced convection were reported previously.[4,5] These experiments have been extended in order to obtain additional data concerning constitutional supercooling of the vapor and the dependence of the growth

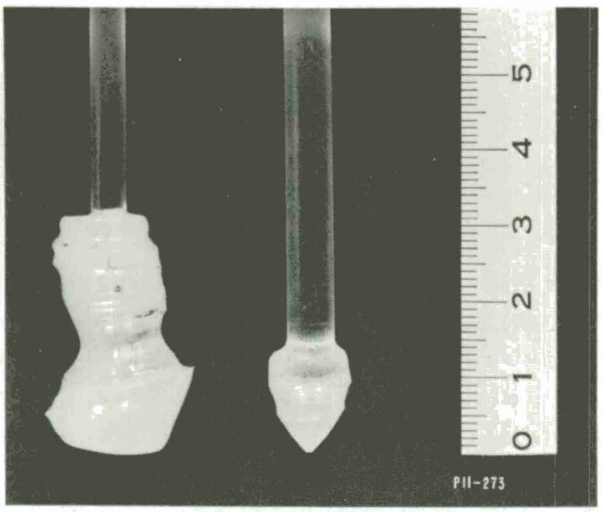

Fig. III-1. Sapphire crystals grown by Czochralski method in a resistance furnace.

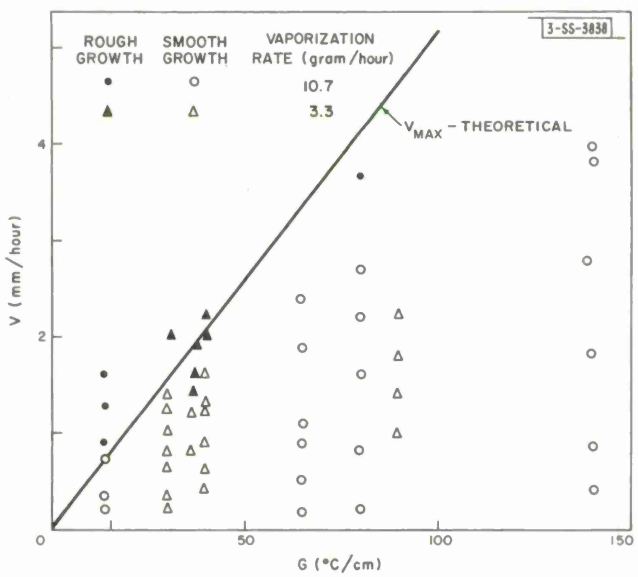

Fig. III-2. Growth velocity v as a function of thermal gradient G for iodine crystals grown from vapor by forced convection. For a fixed value of G, different values of v were obtained by varying helium flow rate and difference between source temperature T_o and interface temperature T_i. Whether growth interface was smooth or rough is indicated for each experimental point. Theoretical curve gives values calculated from Eq. (1) for maximum velocity v_{max} at which growth can occur without constitutional supercooling.

rate on experimental conditions. The experimental procedure was essentially the same as described previously:[5] helium gas was saturated with iodine vapor at temperature T_o, heated to a higher temperature T_2 to produce unsaturation, and then passed around a glass cold finger where condensation occurred at an interface temperature T_i. The growth rate v was measured as a function of $(T_o - T_i)$ and the thermal gradient G in the gas phase. In the present experiments, T_o was 90.0°C and measurements were made at two different helium flow rates, which resulted in iodine vaporization rates of 3.3 and 10.7 gram/hour.

In the earlier experiments, it was found that under given growth conditions the crystal-vapor interface remained smooth only for growth velocities below a certain upper limit. The roughening of the interface which was observed at higher values of v was attributed to constitutional supercooling of the vapor, which theoretical analysis showed to occur when v exceeds a maximum value (v_{max}) given by

$$v_{max} = \frac{MDp_o}{\rho RT^2} \left(\frac{B}{T} - 1\right) G \tag{1}$$

where M is the molecular weight of the condensing species, D is the diffusion constant of the species in the gas phase, $p_o = A \exp[-B/T]$ is the saturated vapor pressure at absolute temperature T, and ρ is the crystal density. The data obtained in the present experiments provide additional confirmation of this explanation. These results are shown in Fig. III-2, where values of v measured under various growth conditions are plotted against G. The theoretical curve in Fig. III-2, which gives values of v_{max} calculated from Eq. (1), is seen to be in good agreement with the experimental boundary between smooth and rough growth.

Values of v for smooth growth as a function of $(T_o - T_i)$ are shown in Fig. III-3. Within the limits of experimental error, v is independent of G for G between 13° and 140°C/cm. The value of v is equal to the rate at which iodine diffuses to the growth interface. If it is assumed that the diffusion layer and thermal boundary layer have the same thickness, it follows from elementary boundary layer theory[6] that

$$v = \frac{KMDV^{1/2}}{\rho RT^2(\nu\ell)^{1/2}} \left[T_i(p_o^o - p_o^i) - p_o^i(T_2 - T_i)\right] \tag{2}$$

where K is a dimensionless constant determined by the geometry of the system, V is the free stream velocity of the gas, ν is the kinematic viscosity of the gas, ℓ is a characteristic length, and p_o^o and p_o^i are the saturated vapor pressures at T_o and T_i, respectively. The theoretical curves shown in Fig. III-3, which give satisfactory agreement with the experimental data, were calculated according to Eq. (2) by adopting 4.9 as the value of K.

According to Eq. (2), v = 0 for $p_o^i = (T_i/T_2)\, p_o^o$ rather than for $p_o^i = p_o^o$, because the growth rate is determined by the concentration gradient in the gas phase, which depends on both the pressure and temperature gradients. For a sufficiently large temperature gradient, Eq. (2) predicts that growth should stop when T_i is still several degrees below T_o. Although some evidence for this result was obtained in the present experiments, it could not be definitely established because of the uncertainty in measuring T_i in the presence of large temperature gradients.

The highest growth velocity achieved in the present experiments was 4 mm/hour. The velocity was limited by the cooling capacity of the cold finger and the maximum rate at which

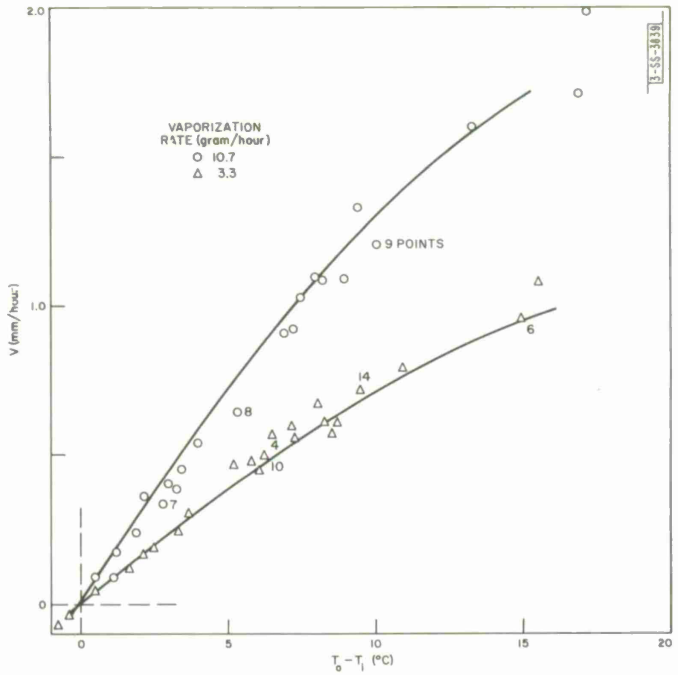

Fig. III-3. Data of Fig. III-2 for smooth growth replotted to show growth velocity v as a function of $(T_o - T_i)$ for iodine crystals grown from the vapor by forced convection. Experimental points do not indicate values of G at which they were obtained. Theoretical curve was calculated from Eq. (2).

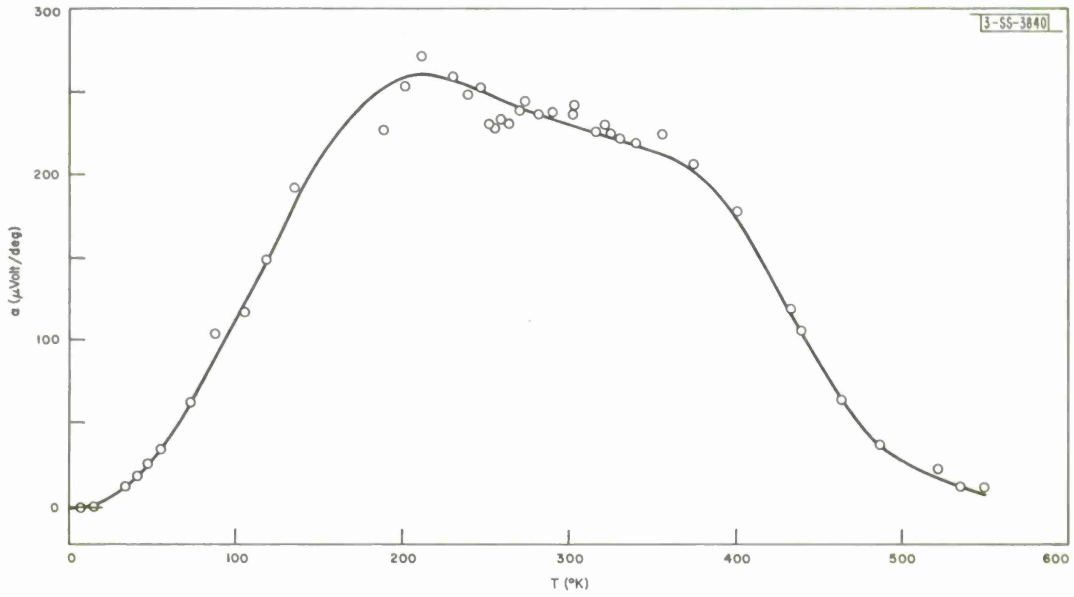

Fig. III-4. Seebeck coefficient α vs absolute temperature T for a single crystal of Ti_2O_3.

iodine could be vaporized without channeling the crystal bed used as the source of vapor. Higher growth rates would be possible if the apparatus were modified to remove these limitations.

T. B. Reed
W. J. LaFleur

C. CRYSTAL GROWTH AND ELECTRICAL PROPERTIES OF TITANIUM SUBOXIDES

Single crystals of Ti_2O_3 (~1 cm^3) and TiO (1 mm^3) have been grown by the Czochralski method in the resistance furnace described in Sec. III-A. The compounds were prepared by reducing well-dried TiO_2 powder with appropriate quantities of powdered titanium metal in argon at 1000°C. Dense material for crucible charges was then obtained by arc-melting. Melts of both compounds could be contained in molybdenum crucibles with little contamination, but tantalum crucibles were immediately destroyed by melts of either type. Considerable difficulty was encountered in pulling crystals more than about 2 cm long, possibly because the thermal gradient in the solid was insufficient to stabilize the growing interface.

Use of an induction plasma torch to grow Ti_2O_3 by the Verneuil method is also being studied. Large-grained boules have been obtained in the initial experiments.

The Seebeck coefficient α of a Ti_2O_3 single crystal has been measured between 7° and 550°K. The results of the measurements are shown in Fig. III-4. At 7°K, $\alpha = -2\,\mu$volt/deg. With increasing temperature α becomes positive, increases to a maximum of about +270 μvolt/deg at 210°K, and then decreases to +12 μvolt/deg at 550°K. A somewhat similar positive maximum was observed by Yahia and Frederikse,[7] who measured α between about 55° and 1200°K.

T. B. Reed R. E. Fahey
J. M. Honig J. T. Roddy

D. CARRIER CONCENTRATIONS AND SUPERCONDUCTIVITY OF In_4SbTe_3

Hall coefficient measurements have been made at 77°K on high- and low-pressure samples of In_4SbTe_3 in an attempt to determine whether their difference in superconducting behavior is due to a difference in carrier concentrations. As previously reported,[8] although there is no detectable difference in structure or composition, samples prepared at high pressure exhibit superconductivity at temperatures below about 1.5°K, but samples prepared at atmospheric pressure or below do not become superconducting down to 1.3°K, the lowest temperature at which measurements have been made.

The Hall coefficient investigation was stimulated by a recent paper by Geller and Hull,[9] who proposed an ionic model to account for the metallic behavior and superconductivity of high-pressure $In_{1-x}Te$(II). According to this model, the lattice contains In^{+1} and In^{+3} ions in the ratio required to balance the charge on the Te^{-2} ions. Thus, stoichiometric InTe(II) contains equal numbers of In^{+1} and In^{+3} ions, while indium-deficient samples contain more In^{+3} than In^{+1} ions. The high-pressure phase is metallic because electrons are easily transferred from one type of indium ion to the other. The concentration of free electrons is equal to twice the concentration of In^{+1} ions and therefore decreases with decreasing indium content. According to Geller and Hull, this decrease in electron concentration accounts for the observed decrease in superconducting transition temperature of $In_{1-x}Te$(II) with decreasing indium content.

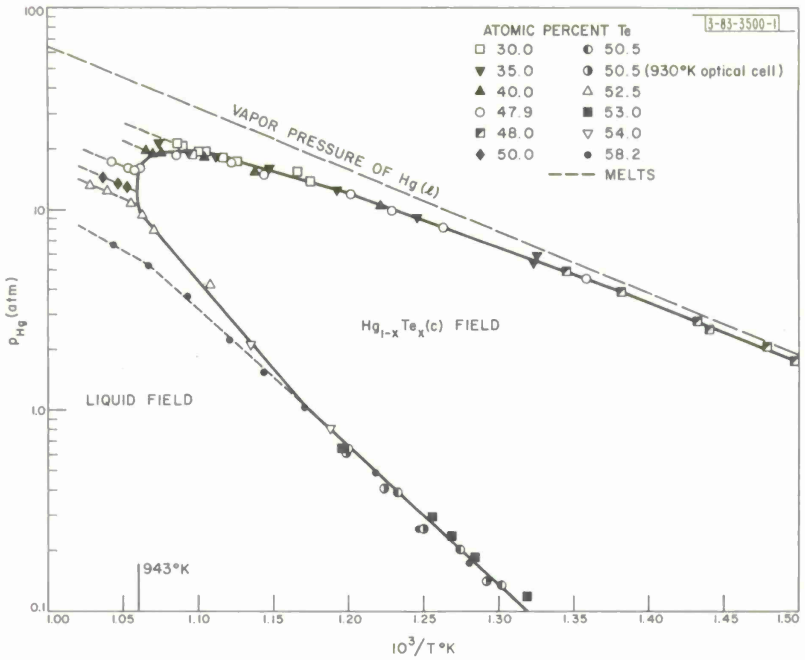

Fig. III-5. Partial pressures of Hg(g) in equilibrium with Hg-Te condensed phases, plotted against reciprocal absolute temperature. Values of p_{Hg} along three-phase lines for HgTe(c) are given by solid curve, those for Hg-Te melts by dashed lines.

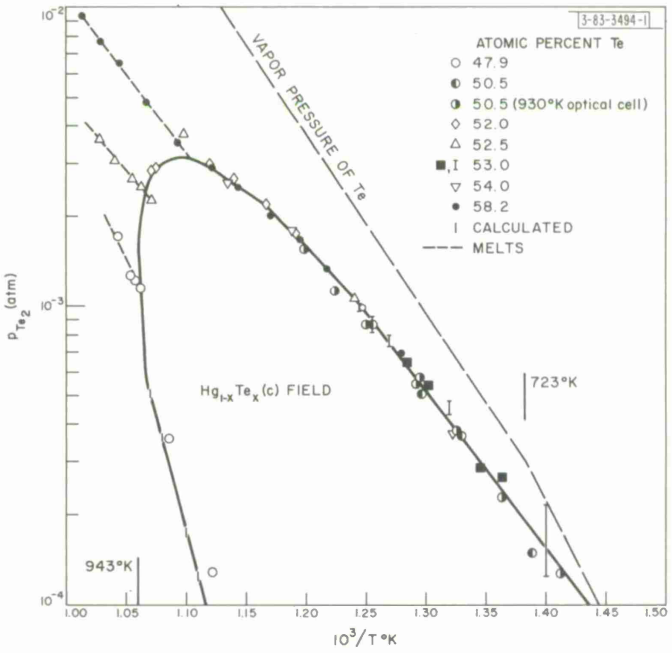

Fig. III-6. Partial pressures of Te_2(g) in equilibrium with Hg-Te condensed phases, plotted against reciprocal absolute temperature. Values of p_{Te_2} along three-phase lines for HgTe(c) are given by solid curve, those for Hg-Te melts by dashed lines.

On the basis of their ionic model, Geller and Hull predicted and prepared a number of superconducting phases related to InTe(II), including $In(Te_{0.67}As_{0.33})$ and $In(Te_{0.5}As_{0.5})$. The analogy between these two materials and In_4SbTe_3, which Geller and Hull did not consider, suggested that the ionic model if valid should also apply to In_4SbTe_3 and that differences in carrier concentration might explain the observed differences in superconducting behavior. As a test of the model, Hall coefficient (R_H) measurements were made at 77°K on three low-pressure and two high-pressure samples. In all cases, R_H is negative, indicating conduction by electrons. The carrier concentrations n calculated from the one-carrier expression $n = -1/R_H e$ are 8.8, 9.0, and 9.4×10^{21} cm^{-3} for the low-pressure samples and 1.1 and 1.2×10^{22} cm^{-3} for the high-pressure samples. The latter values agree rather well with the electron concentration of 1.3×10^{22} cm^{-3} calculated for In_4SbTe_3, according to the ionic model. Furthermore, the observed transition temperatures T_c for the high-pressure samples are 1.4° and 1.5°K, in reasonable agreement with the values of 1.5° to 1.7°K for 1.1 to 1.2×10^{22} cm^{-3}, read from the curve of n vs T_c given by Geller and Hull for $In_{1-x}Te(II)$. The fact that low-pressure samples do not become superconducting down to 1.3°K is also consistent with this curve, which gives $T_c = 1.1$°K for $n = 9 \times 10^{21}$ cm^{-3}. Thus, the model proposed by Geller and Hull accounts for several features of the data. However, since the model predicts that n is determined by composition only, it cannot explain why there is a difference in concentration between the high- and low-pressure samples, which apparently have the same composition. In order to make a further test of the model, it is planned to measure the Hall coefficient as a function of composition for samples of $In_{1-x}Te(II)$ and for high-pressure InTe-InSb alloys containing between 60 and 100 mol % InTe.

M. D. Banus
Lynne B. Farrell
A. J. Strauss

E. PARTIAL PRESSURES OF Hg(g) AND Te_2(g) IN Hg-Te SYSTEM

The partial pressures of Hg(g) and Te_2(g) in equilibrium with Hg-saturated HgTe(c), Te-saturated HgTe(c), and some Hg-Te melts between about 400° and 700°C have been determined by measuring the optical density of the coexistent vapor as a function of wavelength. The optical density measurements were made with a Cary Model 14-H double-beam spectrophotometer, as in our investigation of CdTe (Ref. 10). The relationships between partial pressure and optical density were obtained from the results of calibration experiments on pure mercury and tellurium by using published vapor pressure data for mercury[11,12] and tellurium.[13,14] Values of p_{Hg} were calculated from the measured densities at a number of wavelengths between 2550 and 3100 Å. At these wavelengths, which lie on the long wavelength tail of the mercury absorption line at 2537 Å, the optical densities were found to be proportional to $(p_{Hg})^2$, in agreement with less extensive data reported by Kuhn and Freudenberg.[15] Values of p_{Te_2} were calculated from the measured optical densities at 3650 and 4357 Å, which are proportional to p_{Te_2}. In agreement with mass spectrographic data,[16] the absorption spectra give no evidence for the existence of HgTe(g) molecules.

The measured values of p_{Hg} and p_{Te_2} in equilibrium with condensed phases in the Hg-Te system are plotted against reciprocal absolute temperature in Figs. III-5 and III-6, respectively. The solid lines in each figure are three-phase lines which give the limiting values of partial

TABLE III-1
LIQUIDUS POINTS IN Hg-Te SYSTEM

Condensate Composition (atomic percent tellurium)	Liquidus (°C)
31.1	638
36.1	645
41.8	659
48.5	670
52.8	666
58.7*	628

*Actual tellurium content is slightly higher because of loss of mercury during preparation of optical cell.

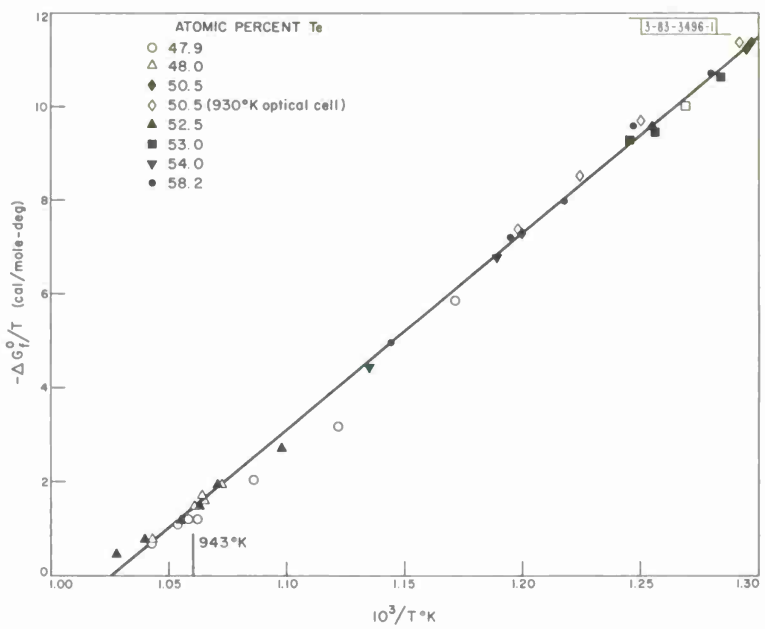

Fig. III-7. Standard Gibbs free energy of formation, divided by absolute temperature, for reaction: Hg (g, 1 atm) + 1/2 Te_2 (g, 1 atm) = HgTe (c, equilibrium vapor pressure).

pressure within which HgTe(c) exists as a stable phase. The partial pressures of both elements are seen to depend strongly on the composition of the solid phase. Partial pressures in equilibrium with Hg-Te melts are indicated by dashed lines. In Fig. III-5, the upper and lower branches of the three-phase curve give values of p_{Hg} in equilibrium with Hg-saturated HgTe(c) and Te-saturated HgTe(c), respectively. The maximum value of p_{Hg} in equilibrium with HgTe(c) is 19 atm. The value of p_{Hg} at the maximum melting point of HgTe(c), 670°C, is about 12.5 atm. In Fig. III-6, the upper and lower branches of the three-phase curve give values of p_{Te_2} in equilibrium with Te-saturated HgTe(c) and Hg-saturated HgTe(c), respectively. The maximum value of p_{Te_2} in equilibrium with HgTe(c) is 3.1×10^{-3} atm.

The partial pressure data for Te-saturated HgTe(c) show that at any temperature p_{Hg} is more than two orders of magnitude greater than p_{Te_2}. Since p_{Hg} has its minimum value and p_{Te_2} has its maximum value for Te-saturated solid, over the temperature range investigated Hg(g) is the predominant vapor species in equilibrium with HgTe(c) of any composition. Thus, over this range, HgTe(c) has no congruently subliming composition, and continued sublimation of any sample will cause sufficient loss of mercury to produce Te-saturated HgTe(c) and eventual formation of a Te-rich liquid phase. Extrapolation of the experimental results shows that this is also true down to at least 300°K.

For any Hg-Te condensate containing HgTe(c) and a liquid phase, with increasing temperature the values of p_{Hg} and p_{Te_2} fall along the three-phase lines of Figs. III-5 and III-6, respectively. At the liquidus temperature, where the condensate becomes entirely liquid, the partial pressures begin to rise above the three-phase lines. If the pressure change is sufficiently abrupt, the liquidus temperature can be determined from the intersection of the three-phase line with the partial pressure line for the melt. Liquidus temperatures obtained in this manner from the data of Figs. III-5 and III-6 are listed in Table III-1. The condensate compositions given have been calculated from the nominal sample compositions by correcting for the preferential loss of mercury to the vapor phase.

The standard Gibbs free energy of formation of HgTe(c), in equilibrium with the vapor phase, from ideal gaseous Hg(g) and Te_2(g), each at 1 atm, is given by ΔG° [HgTe(c)] = RT ln $p_{Hg} p_{Te_2}^{1/2}$, if it is assumed that the vapor phase is ideal and that deviations from stoichiometry are negligible. Values of $\Delta G^\circ/T$ calculated according to this expression from the experimental data for p_{Hg} and p_{Te_2} are plotted against $10^3/T$ in Fig. III-7. The estimated errors due to assuming an ideal vapor phase and stoichiometric solid are insignificant. Most of the values of ΔG° were obtained from data for Te-saturated HgTe(c); those obtained from data for Hg-saturated HgTe(c) are in reasonably good agreement. The variation of ΔG° between 778° and 943°K is well represented by the linear equation ΔG°[HgTe(c)] = $-41.66 + 42.71\ (10^{-3})\ T$ kcal/mole. Extrapolation of this equation to lower temperatures gives values of ΔG° which agree within 6 percent with those obtained by Goldfinger and Jeunehomme[16] from effusion measurements between 435° and 555°K.

R. F. Brebrick
A. J. Strauss

F. WET CHEMICAL ANALYSIS

1. HgTe

A method has been developed for determining mercury and tellurium in HgTe with an accuracy of about one part per thousand. Mercury is determined by direct automatic titration with EDTA to a potentiometric endpoint, using the Reilley gold electrode.[17] The pH is maintained at 4.5 by buffering with sodium acetate-acetic acid. This EDTA titration method is much faster and more accurate than the polarographic method previously developed for mercury in HgTe-CdTe alloys. Tellurium is determined by adding excess potassium dichromate and back titrating with ferrous ammonium sulfate to a potentiometric endpoint.[18]

2. In-Sb-Te System

Methods developed for determining indium, antimony, and tellurium in In-Sb-Te samples have been described previously.[19] The minimum sample size, which was previously 0.5 gram, has now been reduced to 0.2 gram by the use of more dilute titrants (0.01 N) in determining indium and antimony. No reduction in titrant concentration could be made in the tellurium determination, since inconsistent results were obtained with weaker solutions. An accuracy of two parts per thousand in determining each of the three components was obtained in analyses of synthetic standards weighing 0.2 gram.

J. C. Cornwell
E. B. Owens

REFERENCES

1. A.E. Paladino and B.D. Roiter, J. Amer. Ceram. Soc. 47, 465 (1964).
2. O.H. Nestor, "Czochralski Ruby," Annual Summary Report, Union Carbide Corporation, Linde Division, Speedway Laboratories (8 July 1964).
3. Solid State Research Report, Lincoln Laboratory, M.I.T. (1964:3), p. 29.
4. Solid State Research Report, Lincoln Laboratory, M.I.T. (1963:4), p. 33, DDC 435023.
5. Solid State Research Report, Lincoln Laboratory, M.I.T. (1964:2), p. 34, DDC 606126.
6. W.M. Rohsenow and H.Y. Choi, Heat, Mass, and Momentum Transfer (Prentice-Hall, Englewood Cliffs, N.J., 1961), p. 41.
7. J. Yahia and H.P.R. Frederikse, Phys. Rev. 123, 1257 (1961).
8. Solid State Research Report, Lincoln Laboratory, M.I.T. (1964:3), p. 35.
9. S. Geller and G.W. Hull, Jr., Phys. Rev. Letters 13, 127 (1964).
10. R.F. Brebrick and A.J. Strauss, J. Phys. Chem. Solids 25, 1441 (1964).
11. W.T. Hicks, J. Chem. Phys. 38, 1873 (1963).
12. S. Sugawara, T. Sato, and T. Minamiyama, Bull. Jap. Soc. Mech. Eng. 5, 711 (1962).
13. L.S. Brooks, J. Am. Chem. Soc. 74, 227 (1952).
14. A.A. Kudryavtsev and G.P. Ustyugov, Russ. J. Inorg. Chem. 6, 1227 (1961).
15. H. Kuhn and K. Freudenberg, Z. Physik 76, 38 (1932).
16. P. Goldfinger and M. Jeunehomme, Trans. Faraday Soc. 59, 2851 (1963).
17. C.N. Reilley, R.W. Schmidt, and D.W. Lamson, Anal. Chem. 30, 953 (1958).
18. W.J. Schrenk and B.L. Browning, J. Am. Chem. Soc. 48, 139 (1926).
19. Solid State Research Report, Lincoln Laboratory, M.I.T. (1964:2), p. 48, DDC 606126.

IV. BAND STRUCTURE AND SPECTROSCOPY OF SOLIDS

A. INTERBAND TRANSITIONS IN ANTIMONY*

The interband transitions in antimony which have been reported previously[1] have now been studied in more detail. A summary of the results obtained with a binary face in the photon energy range $0.155 < \hbar\omega < 0.305$ ev with the optical electric field E along a bisectrix axis is given in Fig. IV-1. These curves can be experimentally extrapolated to zero field, yielding an energy gap of 0.143 ev. This extrapolation is only approximate, since the lines show curvature, implying nonparabolic energy bands. The reduced effective mass for this series is $\sim 0.018\ m_o$, which again is only an approximation because of the nonparabolic character of the bands. Each oscillation of the series exhibits structure which can be identified with two almost equal effective masses, or with a spin splitting. If the former interpretation is assumed, then the two reduced masses are $\sim 0.016\ m_o$ and $\sim 0.019\ m_o$. The amplitude of these oscillations in the reflectivity is very small for E along the trigonal direction. The corresponding interband transitions on a bisectrix face have also been studied. The reduced effective mass here is approximately equal to that for the binary face and similar polarization effects are found.

A second series of interband transitions is observed for binary, bisectrix, and trigonal faces in the photon energy range $0.105 < \hbar\omega\ 0.175$ ev. Although the band gap associated with these transitions (0.100 ± 0.003 ev) is smaller, the effective masses are heavier and also more anisotropic.

These symmetry considerations suggest that the two sets of transitions occur at different points in the Brillouin zone (see Fig. IV-2) with the larger band gap occurring at point T, and the smaller band gap at point L. A more detailed account of this work has been submitted for publication.

Mildred S. Dresselhaus
J. G. Mavroides

B. ENERGY-MOMENTUM DISPERSION RELATIONS FOR GROUP V SEMIMETALS

The observation of two series of interband transitions in antimony is reported in Sec. IV-A. The band structure calculation of the Group V semimetals[2] indicates that interband transitions are likely to occur about the points L and T in the Brillouin zone. We present here the dispersion relations for the energy bands in the vicinity of these two points.

Of the two, the point L, located at the center of the pseudohexagonal face (see Fig. IV-2), has the lower symmetry, which is designated as C_{2h}. Using $\vec{k} \cdot \vec{p}$ Brillouin-Wigner perturbation theory[3] and the symmetry properties of this point, the energy-momentum relations about this point can be derived. The notation of Ref. 2 is used to label the bands and the representations. The wave vector k_x is taken along the binary axis and transforms as the representation L_3, and the wave vectors k_y and k_z, along the bisectrix and trigonal directions, respectively, transform as the representation L_4. The E vs $\vec{k}$ relation for band L_i is

---

*This experiment was carried out using the high field facilities of the National Magnet Laboratory, M.I.T.

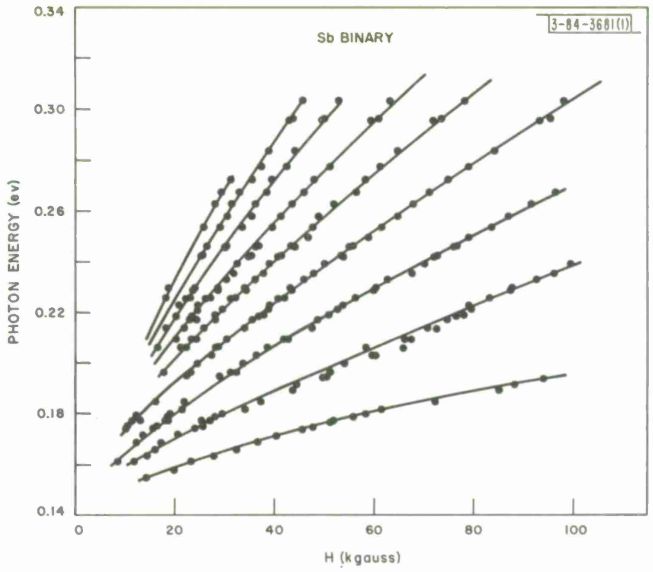

Fig. IV-1. Summary of interband transitions for a binary face. Magnetic field is perpendicular to binary face and optical electric field is along a bisectrix axis. T ~ 4°K.

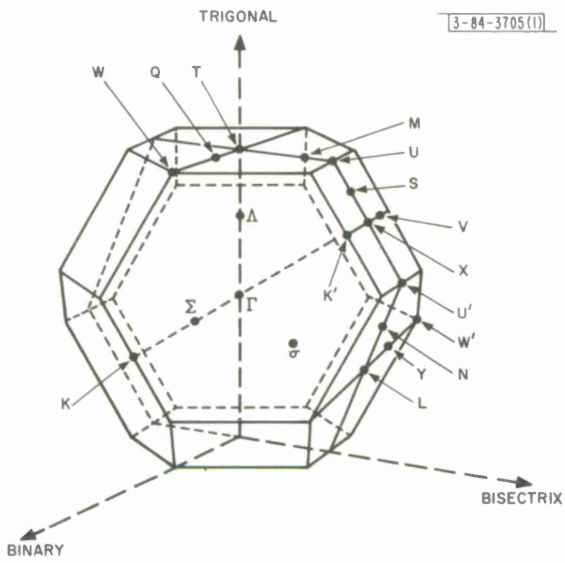

Fig. IV-2. Brillouin zone for a rhombohedral crystal structure, as in antimony. Principal symmetry points and directions are indicated.

$$E_{L_i}(\vec{k}) = E_{L_i}(0) + \frac{\hbar^2 k^2}{2m_o} + \frac{\hbar^2 k_x^2}{m_o^2} \sum_{L_j} \frac{|\pi^x_{i,j}|^2}{E_{L_i}(k) - E_{L_j}(0)}$$

$$+ \frac{\hbar^2}{m_o^2} \sum_{L_j} \frac{|k_y \pi^y_{i,j} + k_z \pi^z_{i,j}|^2}{E_{L_i}(k) - E_{L_j}(0)} \qquad (1)$$

in which the matrix element of the momentum in direction α

$$\pi^{\alpha}_{i,j} = (\psi_i | p_\alpha | \psi_j) \qquad (2)$$

couples only those bands given in Table IV-1. The dispersion relation given in Eq. (2) holds equally well at point X, the center of the rectangular face.

At point T, located at the center of the real hexagonal face, the symmetry follows the group D_{3h}. Here there are four one-dimensional representations (four nondegenerate bands) and two two-dimensional representations (two sets of two doubly degenerate bands). The wave vector k_z along the trigonal direction transforms as $T_{2'}$, while the wave vectors k_x and k_y along the binary and bisectrix directions, respectively, transform as $T_{3'}$. The E vs $\vec{k}$ relations for the four nondegenerate bands can be written as

$$E_{T_i}(\vec{k}) = E_{T_i}(0) + \frac{\hbar^2 k^2}{2m_o} + \frac{\hbar^2 k_z^2}{m_o^2} \sum_{T_j} \frac{|\pi^z_{i,j}|^2}{E_{T_i}(k) - E_{T_j}(0)}$$

$$+ \frac{\hbar^2 (k_x^2 + k_y^2)}{m_o^2} \sum_{T_j} \frac{|\pi_{i,j}|^2}{E_{T_i}(k) - E_{T_j}(0)} \quad . \qquad (3)$$

Table IV-2 defines the momentum matrix elements and lists the selection rules for the terms in these summations.

TABLE IV-1
SUMMARY OF SELECTION RULES AT POINTS L AND X

i \ j	L_1	L_2	L_3	L_4
L_1	0	0	$\pi^x_{1,3}$	$\pi^{y,z}_{1,4}$
L_2	0	0	$\pi^{y,z}_{2,3}$	$\pi^x_{2,4}$
L_3	$\pi^x_{3,1}$	$\pi^{y,z}_{3,2}$	0	0
L_4	$\pi^{y,z}_{4,1}$	$\pi^x_{4,2}$	0	0

TABLE IV-2
SUMMARY OF SELECTION RULES AT POINTS Γ AND T

						T_3		$T_{3'}$	
	i \ j	T_1	$T_{1'}$	T_2	$T_{2'}$	τ_3^+	τ_3^-	$\tau_{3'}^+$	$\tau_{3'}^-$
	T_1	0	0	0	$\pi^z_{1,2'}$	0	0	$1/2k_+\pi_{1,3'}$	$1/2k_-\pi_{1,3'}$
	$T_{1'}$	0	0	$\pi^z_{1',2}$	0	$1/2k_+\pi_{1',3}$	$1/2k_-\pi_{1',3}$	0	0
	T_2	0	$\pi^z_{2,1'}$	0	0	0	0	$1/2k_+\pi_{2,3'}$	$-1/2k_-\pi_{2,3'}$
	$T_{2'}$	$\pi^z_{2',1}$	0	0	0	$1/2k_+\pi_{2',3}$	$-1/2k_-\pi_{2',3}$	0	0
T_3	τ_3^+	0	$1/2k_-\pi_{3,1'}$	0	$1/2k_-\pi_{3,2'}$	0	0	$k_z\pi^z_{3,3'}$	$1/2k_+\pi_{3,3'}$
T_3	τ_3^-	0	$1/2k_+\pi_{3,1'}$	0	$-1/2k_+\pi_{3,2'}$	0	0	$1/2k_-\pi_{3,3'}$	$-k_z\pi^z_{3,3'}$
$T_{3'}$	$\tau_{3'}^+$	$1/2k_-\pi_{3',1}$	0	$1/2k_-\pi_{3',2}$	0	$k_z\pi^z_{3',3}$	$1/2k_+\pi_{3',3}$	0	0
$T_{3'}$	$\tau_{3'}^-$	$1/2k_+\pi_{3',1}$	0	$-1/2k_+\pi_{3',2}$	0	$1/2k_-\pi_{3',3}$	$-k_z\pi^z_{3',3}$	0	0

$k_+ = k_x + ik_y$

$k_- = k_x - ik_y$

The energy relations for the T_3 and $T_{3'}$ bands require the use of degenerate $\vec{k} \cdot \vec{p}$ Brillouin-Wigner perturbation theory. The secular equation

$$\begin{vmatrix} A_i - E_i(k) & B_i \\ B_i^* & A_i - E_i(k) \end{vmatrix} = 0 \tag{4}$$

has roots

$$E_i(k) = A_i \pm |B_i| \tag{5}$$

in which

$$A_i = E_i(0) + \frac{\hbar^2 k^2}{2m_o} + \frac{\hbar^2(k_x^2 + k_y^2)}{4m_o^2} \sum_j \frac{|\pi_{i,j}|^2}{E_i(k) - E_j(0)} + \frac{\hbar^2 k_z^2}{m_o^2} \sum_j \frac{|\pi^z_{i,j}|^2}{E_i(k) - E_j(0)} \tag{6}$$

and

$$B_i = \frac{\hbar^2 k_-^2}{4m_o^2} \sum_j \frac{|\pi_{i,j}|^2}{E_i(k) - E_j(0)} + \frac{\hbar^2 k_z k_+}{2m_o^2} \sum_j \frac{(\pi^z_{i,j}\pi_{j,i} - \text{C.C.})}{E_i(k) - E_j(0)} \tag{7}$$

The dispersion relation given in Eq. (5) holds equally well at point Γ, the center of the Brillouin zone.

In Eqs. (1), (3), and (5), the nonparabolic character of the bands is automatically included in the $\vec{k}$ dependence of the energy denominators. Such nonparabolic effects have been shown to be important in bismuth (Ref. 4) and antimony (Ref. 5). The effect of spin-orbit interaction can easily be included in this formalism and, in particular, is important in lifting the degeneracy of the T_3 and $T_{3'}$ bands.

These dispersion relations are being applied to explain the magnetoreflection experiments reported in Sec. IV-A.

G. Dresselhaus
Mildred S. Dresselhaus

C. MAGNETOPLASMA EFFECTS IN BISMUTH

In studying the magnetoplasma effects in antimony it was found by Dresselhaus and Mavroides[6] that a simple three-tilted ellipsoidal model failed to give even qualitative agreement with experiment. Further investigation indicated that the onset of direct interband transitions occurred near the plasma edges suggesting that the observed incorrect sign and amplitude for the magnetoplasma effect as a function of energy for certain orientations was probably due to these interband effects. In order to establish the validity of the free multicarrier model calculation, experiments are now being carried out on the semimetal bismuth which has a multi-ellipsoidal Fermi surface somewhat like antimony and, in addition, the further simplification that the direct interband transitions in bismuth occur at much higher photon energies than the energies corresponding to the plasma frequencies. Preliminary results of this magnetoreflection previously reported by Boyle and Brailsford[7] are not detailed enough to allow a comparison with

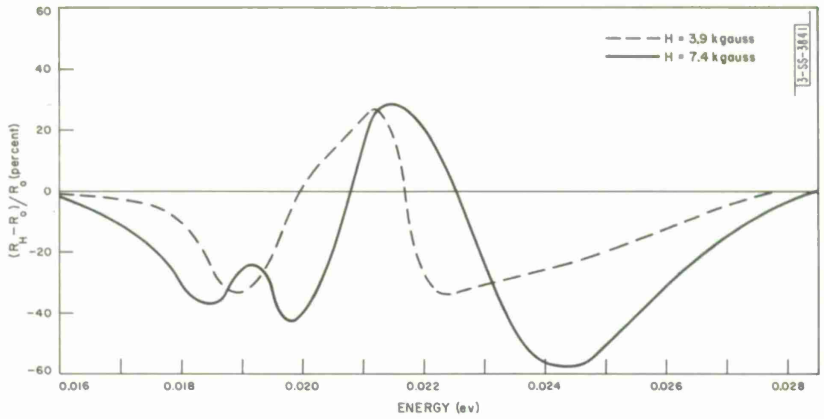

Fig. IV-3. Variation of optical reflectivity with photon energy for H = 3.9 kgauss and H = 7.4 kgauss. Light is incident on binary face and magnetic field is parallel to a bisectrix axis.

the calculations. Figure IV-3 indicates the magnetoplasma effects measured with unpolarized light incident on a binary face with the magnetic field parallel to a bisectrix axis. It will be noted that there is a rather complex dependence on both photon energy and magnetic field. The proper use of polarized radiation is expected to allow the examination of each plasma edge separately.

D. H. Dickey

D. FARADAY ROTATION OF INDIRECT TRANSITION IN GERMANIUM*

We have observed on transmission the oscillatory Faraday rotation of the indirect transition in germanium. These preliminary observations were made at magnetic fields of 62 kgauss and at helium temperatures on a heat sunk sample. From the position of the indirect gap the temperature was determined as 15°K. The sample was intrinsic, with a carrier concentration $n < 10^{13}/cm^3$. The data were taken with the magnetic field (and the direction of propagation) perpendicular to a (110) face.

Comparison of the Faraday rotation with the corresponding transmission as a function of wavelength shows that there are oscillatory curves corresponding to both the exciton absorption and to the Landau steps. The entire indirect transition rotation is superposed on a very large dispersive tail which probably arises from the $\Gamma_{25'} \rightarrow \Gamma_{2'}$ direct energy gap transition. At the temperatures and magnetic fields in question the oscillatory effects are of the order of 2 percent of the total rotation.

Since the Faraday rotation is a dispersive effect and the direct and indirect contributions at a given wavelength are superposed, one should be able to make a direct comparison of the matrix elements involved in the respective transitions. Calculations are presently being carried out toward this end.

J. Halpern

* This experiment was carried out using the high field facilities of the National Magnet Laboratory, M.I.T.

E. EXCITON ABSORPTION IN GaSb*

Exciton lines have previously[8] been observed in GaSb. Some of these have been attributed to the formation of complexes consisting of an ionized acceptor ion and an exciton. Similar lines in III-V compounds have been observed in emission in GaAs (Sec. IV-G) and InAs (Ref. 9). For such a complex the calculation of energy levels and their dependence on magnetic field appears to be rather difficult. The study of the absorption lines under the influence of magnetic field and under the influence of strain may provide an understanding of the energy levels that can lead to a solution of the theoretical problem.

Previous work[10] has shown that the diamagnetic effect on the absorption lines ($H \lesssim 20$ kgauss) is quadratic and is the same as that on the free exciton. A spin splitting is observed which appears to be due to the spin of the electron associated with the complex. Magnetic field measurements on the γ line (Ref. 8) have been extended to ~90 kgauss. The functional behavior of the diamagnetic shift changes beyond 20 kgauss and eventually becomes linear. The critical field for free excitons in GaSb is ~20 kgauss and the observed behavior agrees with that predicted by the theory of Elliott and Loudon.[11] Analysis of the observed shift yields a reduced electron-hole effective mass of 0.051 m_o which may be compared to the value of 0.042 m_o reported previously.[12] These results substantiate the earlier indication that the diamagnetic effect of the associated exciton-impurity complex is the same as that of the free exciton.

The observed splitting corresponds to $|g| = 10.3$ which is slightly higher than the value of $|g| = 9.4$ obtained below 20 kgauss and may indicate a slight increase in $|g|$ with magnetic field.

Changes in the spectra below 20 kgauss with change in the polarization of the light indicates structure due to splitting in the valence band. The splittings in the absorption lines in fields up to ~90 kgauss were too small to be resolved.

E. J. Johnson
G. B. Wright

F. OPTICAL ABSORPTION BY EXCITONS

The probability per unit time that, with a radiation density $\rho(\nu)$ of frequency ν, a crystal will make an electronic transition from the ground state Ψ_o to an excited (exciton) state $\Psi^{n,K}$ is given by

$$W = \frac{1}{\hbar\nu^2} \left| \langle \Psi^{n,K} \right| \sum_i \exp[i\vec{q} \cdot \vec{r}_i] \, \vec{\xi} \cdot \vec{j}_i \left| \Psi_o \rangle \right|^2 \rho(\nu) \, \delta(E - E_o + h\nu) \qquad (8)$$

where $\vec{q}$ and $\vec{\xi}$ are the wave vector and polarization vector of the photon, respectively, and $\vec{j}_i$ is the current operator for the i^{th} electron at the position $\vec{r}_i$. In order to evaluate Eq. (8) we must calculate the matrix element $\langle \Psi^{n,K} | \sum_i \exp[i\vec{q} \cdot \vec{r}_i] \, \vec{\xi} \cdot \vec{j}_i \, | \Psi_o \rangle$. This has been done by Elliott[13] in the limit of small wave vector ($q = 0$). In the general case of degenerate conduction and valence bands the result in this limit is

*This experiment was carried out using the high field facilities of the National Magnet Laboratory, M.I.T.

$$\langle \Psi^n | \sum_i \vec{\xi} \cdot \vec{j}_i | \Psi_o \rangle = V^{1/2} \sum_{i=1}^{s} \sum_{j=1}^{t} \left\{ \bar{\psi}^n_{c_i v_j}(\vec{r}) \Big|_{r=0} + \left[-i \nabla_r^\alpha \bar{\psi}^n_{c_i v_j}(\vec{r}) \right]_{r=0} \nabla_k^\alpha \right.$$

$$+ \frac{1}{2} \left[(-i\nabla_r^\alpha)(-i\nabla_r^\beta) \bar{\psi}^n_{c_i v_j}(\vec{r}) \right]_{r=0} \nabla_k^\alpha \nabla_k^\beta$$

$$\left. + \ldots \right\} \langle \psi_{c_i k} | \vec{\xi} \cdot \vec{j} | \psi_{v_j k} \rangle \Big|_{k=k^o} \tag{9}$$

where i and j run over the s degenerate conduction bands and t degenerate valence bands, respectively, $\bar{\psi}^n_{c_i v_j}(\vec{r})$ is a solution of a set of s times t simultaneous differential equations (exciton effective mass equations;[14] $\vec{r}$ is the relative coordinate of the electron and hole and Eq. (9) is evaluated at r = 0; α and β run over the directions x, y, and z and the operators ∇_k^α take the derivative of the band-to-band matrix element $\langle \psi_{c_i k} | \vec{\xi} \cdot \vec{j} | \psi_{v_j k} \rangle$ with respect to a variation of k^α evaluated at $\vec{k} = \vec{k}^o$ the location in k-space of the direct band-to-band transition.

For finite wave vector q and in the presence of external magnetic fields we have found the generalization of Eq. (9) to be,

$$\langle \Psi^{n,K} | \sum_i \exp[i\vec{q} \cdot \vec{r}_i] \vec{\xi} \cdot \vec{j}_i | \Psi_o \rangle = V^{1/2} \sum_{i=1}^{s} \sum_{j=1}^{t} \left\{ \bar{\psi}^{n,K}_{c_i v_j}(\vec{r}) \Big|_{\substack{r=0 \\ K=q}} \right.$$

$$+ \left[-iD^\alpha \bar{\psi}^{n,K}_{c_i v_j}(\vec{r}) \right]_{\substack{r=0 \\ K=q}} \nabla_k^\alpha + \frac{1}{2} \left[(-iD^\alpha)(-iD^\beta) \bar{\psi}^{n,K}_{c_i v_j}(\vec{r}) \right]_{\substack{r=0 \\ K=q}}$$

$$\left. \times \nabla_k^\alpha \nabla_k^\beta + \ldots . \right\} \langle \psi_{c_i,\, k+q/2} | \exp[i\vec{q} \cdot \vec{r}] \vec{\xi} \cdot \vec{j} | \psi_{v_j,\, k-q/2} \rangle_{k=k^o} \tag{10}$$

where the operator $\vec{D}$ is given by

$$\vec{D} = \frac{e}{2\hbar c} \vec{H} \times \vec{\nabla}_K + \vec{\nabla}_r \tag{11}$$

where $\vec{\nabla}_K$ takes the derivative of $\bar{\psi}^{n,K}_{c_i v_j}$ with respect to K. $\bar{\psi}^{n,K}_{c_i v_j}$ is an implicit function of K since the Hamiltonian of which $\bar{\psi}^{n,K}_{c_i v_j}$ is an eigenfunction depends on K (Ref. 14). In addition, the only difference between Eq. (10) and Eq. (9) is that whereas in Eq. (9) the conduction and valence band functions were both evaluated at $\vec{k} = \vec{k}^o$ in Eq. (10), the conduction and valence band functions are evaluated at $\vec{k} = \vec{k}^o + 1/2\vec{q}$ and $\vec{k} = \vec{k}^o - 1/2\vec{q}$, respectively, in terms of an expansion about k^o. That is, we write

$$\psi_{c_i,\, k^o+q/2} = \exp[i(\vec{k}^o + \tfrac{1}{2}\vec{q}) \cdot \vec{r}]\, u_{c_i,\, k^o+q/2} \tag{12}$$

and

$$u_{c_i,\, k^o+q/2} = u_{c_i,\, k^o} + \frac{1}{2} \vec{q} \cdot \vec{\nabla}_k u_{c_i,\, k^o} + \ldots \tag{13}$$

and similarly for $\psi_{vj,\, k^o-q/2}$. Therefore, the matrix element $\langle \Psi^{n,K} | \sum_i \exp[i\vec{q} \cdot \vec{r}_i]\, \vec{\xi} \cdot \vec{j}_i \, | \Psi_o \rangle$ can be easily obtained as an expansion in powers of $\vec{q}$ from Eq. (10).

J. O. Dimmock

G. PHOTOLUMINESCENCE OF GaAs IN A HIGH MAGNETIC FIELD*

The photoluminescence of GaAs has been studied. The lines observed in n-type material included those reported at zero field by Nathan and Burns.[15] The exciton lines and several transitions proceeding through holes trapped at acceptors all exhibited the same variation of photon energy with magnetic field. The energy shift, which was quadratic at low fields and linear at high fields, could be described by a simple effective mass hydrogenic model with an effective mass for the electron of about 0.06 m_o, and a binding energy of approximately 5 mev. The binding energy required for the fit changed very little with the zero-field photon energy of the emission lines, which in some cases was as much as 200 mev below the energy gap of GaAs. Evidently, the binding energy of the trapped hole had little effect on the magnetic behavior of the recombination radiation. Attempts to resolve a spin splitting due to holes were unsuccessful for any of the transitions. The g-factors for holes on zinc and cadmium impurities reported by Title[16] for strained samples would have given rise to splittings well within the resolution capabilities of the instrument. In fact, a fourfold splitting of the exciton line in CdTe has been observed.

In the n-type material studied, the intensity of the lines was practically unaffected by the magnetic field. In p-type material, however, an additional line was observed, and as the magnetic field increased, this line shrank, while the other lines grew, sometimes as much as tenfold in intensity. Evidently, the field was changing the relative electron capture cross sections for the various centers involved. The magnitude of the effect was not reproducible with time.

G. B. Wright
F. L. Galeener†

H. PIEZOELECTRIC POLARONS IN STRONG MAGNETIC AND COULOMB FIELDS

Recently reported measurements[17,18] of the cyclotron resonance frequency of electrons in the conduction band of CdS seem to indicate that the Landau levels are approximately 20 percent more widely separated than is to be expected on the basis of the electronic effective mass. A theory which purports to explain this anomaly on the basis of piezoelectric electron-phonon interaction has been proposed by Hopfield and Mahan,[19] but this theory is subject to grave criticism on theoretical grounds.

Like Hopfield and Mahan, we have used a Fröhlich-type Hamiltonian with an isotropic electron-phonon interaction term to serve as a model for the piezoelectric electron-phonon coupling. However, we have studied the effects of such coupling on the electron energy at zero temperature (where the lowest order perturbation theory can be rigorously evaluated) in the presence of (1) a uniform external magnetic field H, and (2) a coulomb potential binding the electron to a fixed center.

---

* This experiment was carried out using the high field facilities of the National Magnet Laboratory, M.I.T.

† National Magnet Laboratory, M.I.T.

In CdS, the dimensionless piezoelectric coupling constant $\tilde{\alpha}$, defined so as to play the same role as Fröhlich's α plays in the usual polaron theory,[20] is found to be approximately 0.2 (using Hutson's data).[21]

Therefore, we have treated the electron-phonon interaction in lowest-order perturbation theory in the presence of a strong magnetic field in order to determine the perturbation of the energy spacing between the n = 1 and n = 0 Landau levels at zero temperature. In the limit of infinite field, the spacing is found to increase by an amount proportional to $H^{1/4}$. However, for magnetic fields readily attainable in the laboratory, it is necessary to evaluate the perturbation expression numerically. Preliminary results indicate that for field strengths of the order of several kilogauss the piezoelectric interaction in this model is much too weak to account for the 20-percent effect observed.

If we denote the discrete index which labels the energy of an electron in a magnetic field by n, then we find that the "golden rule" expression for the decay probability of electron levels, which can emit a phonon without change of n and still conserve energy in the process, diverges. Closer analysis shows that lowest-order perturbation theory implies that the decay is nonexponential in time. The consequences for the line shift at temperatures above zero need further investigation.

The effect of the piezoelectric electron-phonon interaction on the ionization energy of an electron bound in a coulomb field to a point center of charge is to increase the ionization energy by a percentage which is independent of the strength of the coulomb field for strong fields. In CdS this should be approximately a 2-percent effect.

Interesting results for upper and lower limits of the ground state energy of a polaron bound in a coulomb field have been obtained.

D. M. Larsen

I. CALCULATION OF RELATIVISTIC ENERGY BANDS IN CRYSTALS

In connection with a continuing interest in the band structure of rare earth metals[22] we have obtained a formal solution of the relativistic Schrödinger equation for the periodic "muffin tin" potential in the framework of the augmented plane-wave (APW) method.[23] The problem of evaluating the relativistic solution for specific materials does not appear to be much more difficult than that of evaluating the nonrelativistic solution. The principal inaccuracies in the relativistic calculation are still, as in the nonrelativistic calculation, due to inaccuracies in the assumed effective potential. Disregarding these errors, it appears possible to obtain solutions of the relativistic periodic potential problem to an accuracy of about $\pm 0.001\,R_y$ with present day computers. This would result in the calculation, directly using an APW method, of spin-orbit splittings and other relativistic effects in solids directly. The method appears quite feasible and attention is now being given to the problems of programming the calculation to obtain relativistic energy bands in some specific materials.

J. O. Dimmock

J. OPTICAL STUDIES ON SULFUR-DOPED SILICON

We have been studying the optical properties of sulfur-doped silicon.[24] By suitably choosing the starting material and thermal treatment, one can obtain samples with sulfur impurities existing as neutral single sulfur atoms, singly ionized single sulfur atoms, or as singly ionized

sulfur pairs. The absorption lines due to sulfur in silicon are shown in Fig. IV-4, where a bracket indicates a group of lines due to a given type of sulfur center. When these absorption lines were studied under stress it was found that all the absorptions due to transitions between a ground state and the excited p-like states had identical shifts. Figure IV-5 shows the splitting and the shift of energies of the transitions to p-like states under an applied stress in the [001] direction for each type of sulfur center. Measurements were also made using polarized light. Figure IV-6 shows the absorption spectra of the neutral single sulfur atoms at zero stress, and at a stress of 2.24×10^8 dynes/cm^2 for light polarized both parallel and perpendicular to the applied stress.

For a uniform longitudinal stress $\overleftrightarrow{T} = T\hat{m}\hat{m}$, where $\hat{m}$ is a unit vector along the stress axis with components m_x, m_y, and m_z referred to the cube axes of the crystal, the minimum of the j^{th} valley of the conduction band in silicon shifts by

$$\delta E^{(j)} = E_1(s_{11} + 2s_{12})\, T + E_2(s_{11} - s_{12})\,(m^2_{|j|} - \tfrac{1}{3})\, T \qquad (14)$$

where j = x, $\bar{x}$, y, $\bar{y}$, z, $\bar{z}$; E_2 is Brook's notation[25] for the pure shear deformation potential coefficient of a valley, which is denoted by Herring and Vogt[26] by Ξ_u; and s_{11} and s_{12} are the standard elastic compliance coefficients. Equation (14) assumes that the shift in energy of a valley minimum depends linearly on the strain (or the stress). In the effective mass approximation, strain will shift the donor levels in this manner when intervalley coupling is negligible. When T is parallel to the [001] direction, the equation for the splitting of a p-state reduces to the form

$$E_2 = \frac{\delta E^{(z,\bar{z})} - \delta E^{(x,\bar{x},y,\bar{y})}}{(s_{11} - s_{12})\, T} \qquad (15)$$

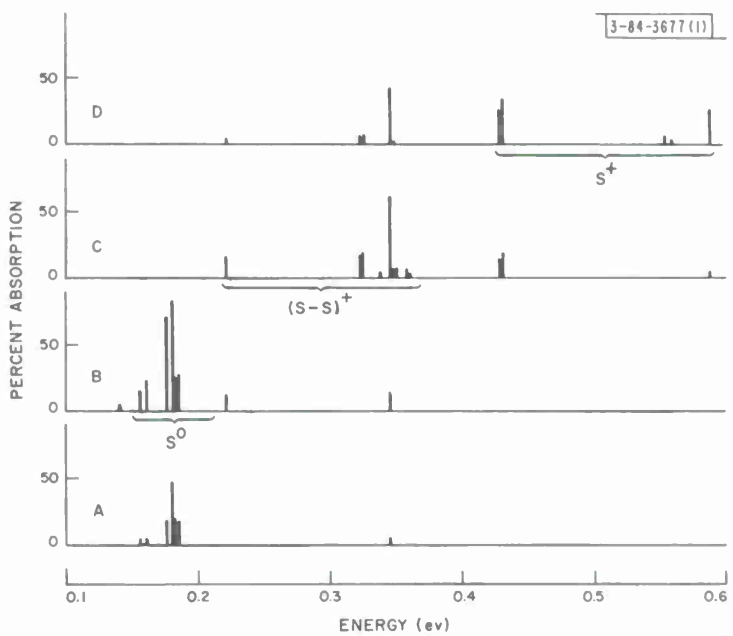

Fig. IV-4. Absorptions in sulfur doped silicon for samples with various starting materials and thermal treatments.

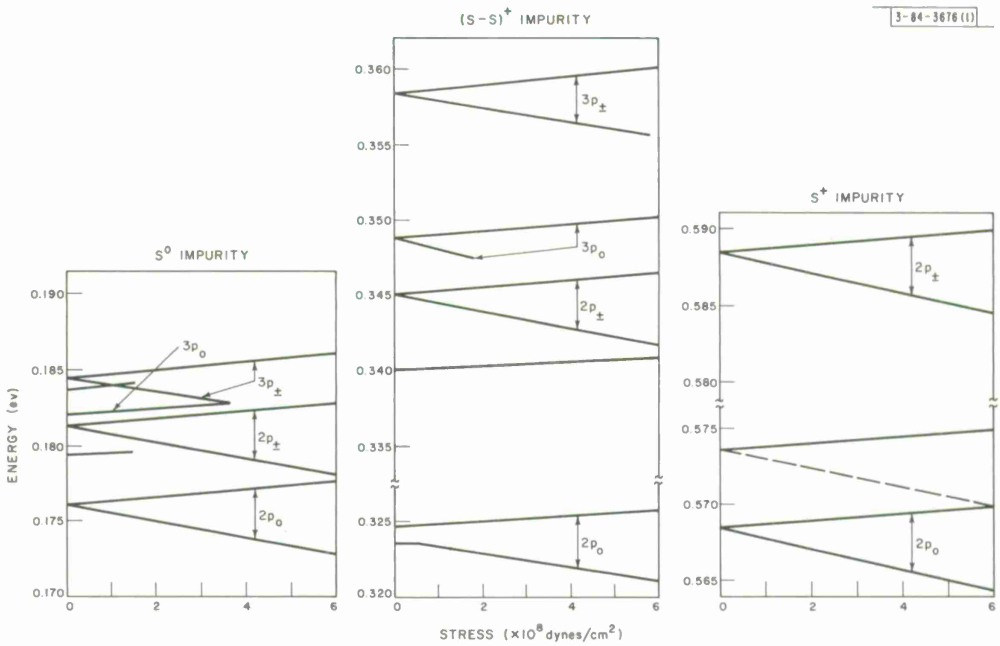

Fig. IV-5. Effects of stress on transitions to p-like states for three types of sulfur impurity centers.

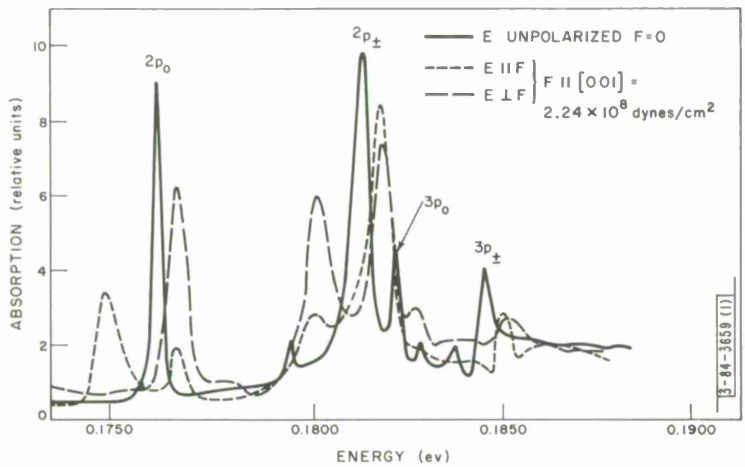

Fig. IV-6. Effect of stress on S^0 impurity spectrum in silicon.

Using this equation, and substituting the measured value for the splitting of the p-like states under stress, and Fine's value[27] of $(s_{11} - s_{12})^{-1} = 1.016$ dynes/cm^2, we obtain the value $E_2 = 7.9 \pm 0.2$ ev.

W. E. Krag H. J. Zeiger
W. H. Kleiner S. Fischler

K. UNUSUALLY LARGE ELECTRON HALL MOBILITY, MAGNETORESISTANCE AND MAGNETO-HALL EFFECTS IN HgTe

Hall coefficients R and magnetoresistance $\Delta\rho/\rho_o$ have been measured at 4.2° and 78°K on a variety of HgTe samples in magnetic fields H ranging from 0.4 to 105 kgauss. The dependence of R on H for a selected set of samples is shown in Fig. IV-7, and the key data pertaining to these and other samples are summarized in Table IV-3 in order of decreasing estimated ratios of electron n to hole p concentrations. Sample A is typical of an extrinsic n-type material below 78°K. Corresponding to a large n/p ratio, R is negative and independent of H and $\Delta\rho/\rho_o \approx 1$. As one proceeds to smaller n/p ratios in samples B through E, the low field Hall coefficients R(o) pass through a deep minimum of about -3000 cm^3/coulomb, and $\Delta\rho/\rho_o \gg 1$. The large numerical values of R at 4.2°K in low magnetic field are consistent with the overlap band model of HgTe (Ref. 28), since the electron to hole mobility ratios are large and $n/p < 1$. Also, for the range of n/p values encountered in samples D to F, R(H) at 4.2°K changes from negative to positive with increasing H. This behavior is expected for a material with an

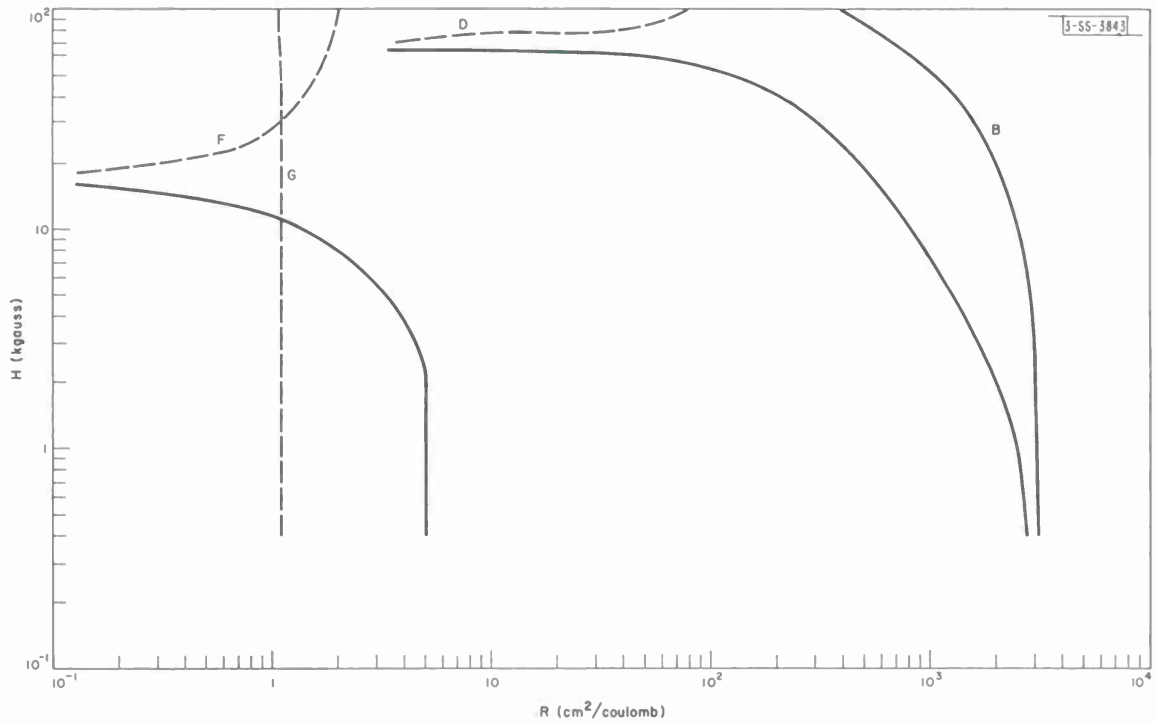

Fig. IV-7. Experimental curves of Hall coefficient R vs magnetic field strength for samples B, D, F, and G of HgTe. Solid curves designate negative Hall coefficients, whereas dashed curves denote positive R. (High field measurements were made at the National Magnet Laboratory, M.I.T.)

overlapped band model. Sample G is typical of extrinsic, p-type material; here $n/p \to 0$, $R > 0$ for all H, and $\Delta\rho/\rho_o < 1$.

It is of interest that samples for which $R > 4$ cm^3/coulomb have not been encountered. This is in agreement with theoretical predictions which place an upper limit on positive R for semimetals with large electron to hole mobility ratios.

The results cited can be qualitatively understood as follows: In sample A the Fermi level E_F is at least 4kT above the valence band (VB) edge; hence, only electrons contribute to transport properties. Sample B is nearly intrinsic; here, E_F lies below the top of the VB, so that both holes and electrons participate in conduction, rendering $\Delta\rho/\rho_o \approx 200$ at 105 kgauss. In passing from sample C to G, E_F systematically diminishes until it is more than 4kT below the bottom of the conduction band edge. At 4.2°K, only holes conduct in sample G; however, the thermal spread in electron energies at 78°K is sufficient to enable high mobility electrons to participate, thus making $R(o) < 0$ at this temperature. Positive R were encountered both at 4.2° and 78°K for samples more heavily doped by p-type impurities than sample G.

Table IV-3 shows that electron Hall mobilities in excess of 350,000 cm^2/volt-sec have been observed at 4.2°K. These values are higher than any mobilities reported for HgTe to date and are in excess of the mobilities cited for any zinc blende material, including InSb, at this temperature. These high electron mobilities are not due to the large static dielectric constant as in PbTe but are associated with the low electron effective mass and the fairly high state of purity of the material under study.

Attempts to fit these data quantitatively to a mixed conduction model are in progress.

T. C. Harman
J. M. Honig
A. E. Paladino

L. THERMAL ENERGY GAP OF HgTe

The thermal energy gap of HgTe has been determined from data on the Hall coefficient R by the same method previously used to find the thermal energy gap of HgSe (Ref. 29). The data were obtained in experiments on n-type samples with net donor concentrations between 2×10^{16} and 5×10^{18} cm^{-3} as determined from Hall coefficient measurements at 4.2°K. (By definition, a material is n-type if $n > p$ and p-type if $p > n$.) These samples, which were cut from large-grained ingots grown from iodine-doped melts by the Bridgman technique, were mercury saturated by annealing at 350°C to reduce the concentration of acceptor defects resulting from stoichiometric deviations. Identification of samples as n-type was based on values of resistivity and Hall coefficient measured at 300°, 77°, and 4°K for various values of magnetic field strength. This detailed identification was necessary because some p-type samples of HgTe have negative Hall coefficients even at 4°K, since the ratio of electron mobility μ_n to hole mobility μ_p is at least 100 in HgTe (Ref. 30). Because of this high mobility ratio, the electron concentration in an intrinsic or n-type sample at any temperature is given by the usual expression for one-carrier conduction: $n = -1/Rec$. For all n-type samples, the electron concentration either remained essentially constant or first remained constant and then increased monotonically with increasing temperature from 4° to 300°K. The increase in concentration is due to thermal excitation of electrons from a valence band rather than from a partially ionized donor level.

TABLE IV-3

SUMMARY OF PERTINENT DATA FOR SAMPLES A TO G

Sample No.	Sample Type	$R_4(0)^*$	$\rho_4(0)^\dagger$	$^{\mu}H_4{}^{\ddagger}$	$\Delta\rho/\rho(0)_4{}^{\S}$	$R_{78}(0)^*$	$\rho_{78}(0)^\dagger$	$^{\mu}H_{78}{}^{\ddagger}$
A	N	−40	5.3×10^{-4}	7.6×10^{4}	≈1	−40	5.6×10^{-4}	7.1×10^{4}
B	P	−3000	8.4×10^{-3}	3.6×10^{5}	200	−98	1.2×10^{-3}	8.2×10^{4}
C	P	−1500	1.5×10^{-2}	1×10^{5}	–	−47	1.1×10^{-3}	4.3×10^{4}
D	P	−2800	3.3×10^{-2}	3.6×10^{4}	27	−99	2.1×10^{-3}	4.7×10^{4}
E	P	−960	1.2×10^{-2}	8×10^{4}	–	−66	7.5×10^{-3}	8.8×10^{3}
F	P	−5	1.4×10^{-2}	2.9×10^{2}	<1	−15	1.3×10^{-2}	1.2×10^{3}
G	P	+1.1	2.1×10^{-2}	52	<1	−5	1.6×10^{-2}	3.1×10^{2}

* Weak field Hall coefficient at 4° and 78°K in cm^3/coulomb.

† Electrical resistivity for zero magnetic field at 4° and 78°K in ohm-cm.

‡ Hall mobility at 4° and 78°K in cm^2/volt-sec.

§ Magnetoresistance for a magnetic field of 105 kgauss at 4°K.

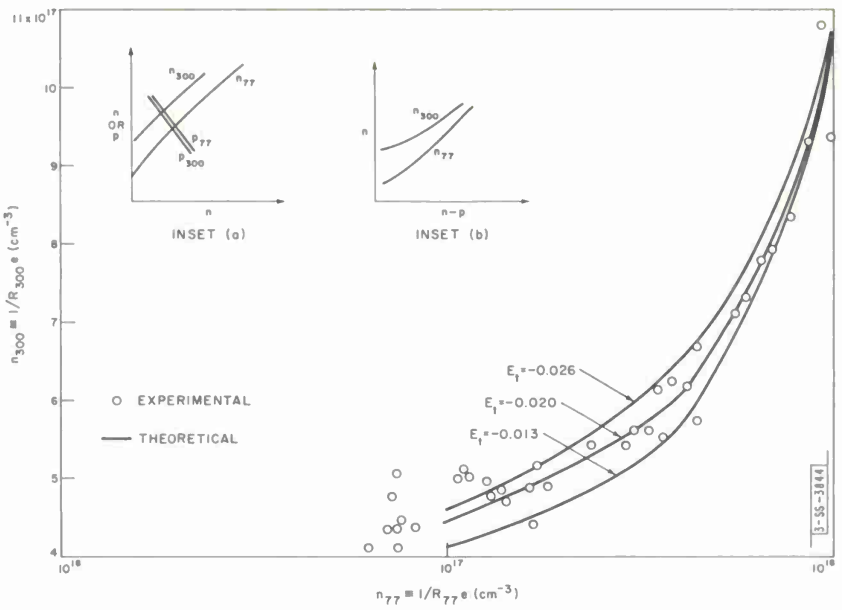

Fig. IV-8. Experimental and theoretical values of electron concentration at 300°K(n_{300}) vs electron concentration at 77°K(n_{77}) for HgTe. Theoretical values were calculated using $m_p^{(N)} = 0.16$, $E_G = 0.14$ ev, $P = 6.5 \times 10^{-3}$ ev-cm, and the values of E_t given in the figure.

The initial theoretical plot of n_{300} vs n_{77} did not agree satisfactorily with experiment, since the values of E_t and $m_p^{(N)}$ were only preliminary. In order to obtain better agreement, the procedure described above was repeated with different combinations of E_t and $m_p^{(N)}$ values. The best fit to the data was obtained for $m_p^{(N)} = 0.16\, m_o$. The degree of agreement is shown in Fig. IV-8, which gives the experimental results and theoretical curves for $m_p^{(N)} = 0.16\, m_o$ and three values of E_t. Because of the sensitivity of the calculated results to the value of E_t, it can be concluded that $E_t = -0.02 \pm 0.01$ ev. For HgSe, values of $E_t = -0.07$ ev and $m_p^{(N)} = 0.17\, m_o$ were obtained previously.[29]

T. C. Harman
A. J. Strauss
S. Hilsenrath

REFERENCES

1. Solid State Research Report, Lincoln Laboratory, M.I.T. (1964:3) p.39.
2. M.H. Cohen, L.M. Falicov, and S. Golin, IBM J. Research Develop. 8, 215 (1964).
3. G. Dresselhaus, PhD Thesis, University of California 1955 (unpublished).
4. B. Lax and J.G. Mavroides, Advances in Solid State Physics, F. Seitz and D. Turnbull, eds. (Academic Press, New York, 1960), Vol.11.
5. M.S. Dresselhaus and J.G. Mavroides (to be published).
6. Solid State Research Report, Lincoln Laboratory, M.I.T. (1964:1), p.42, DDC 601830.
7. W.S. Boyle and A.D. Brailsford, Phys. Rev. 120, 1943 (1960).
8. E.J. Johnson and H.Y. Fan, Bull. Am. Phys. Soc. 7, 185 (1962); E.J. Johnson, I. Filinski, and H.Y. Fan, Proceedings of the International Conference on the Physics of Semiconductors, Exeter (1962), p.375.
9. F.L. Galeener, I. Melngailis, G.B. Wright, and R.H. Rediker, J. Appl. Phys. (in press).
10. E.J. Johnson, PhD Thesis, Purdue University (1964); E.J. Johnson and H.Y. Fan (to be published).
11. R.J. Elliott and R. Loudon, J. Phys. Chem. Solids 8, 382 (1959).
12. S. Zwerdling, B. Lax, K.J. Button, and L.N. Roth, J. Phys. Chem. Solids 9, 320 (1958).
13. R.J. Elliott, Phys. Rev. 108, 1384 (1957).
14. G.F. Dresselhaus, J. Phys. Chem. Solids 1, 14 (1956).
15. M.I. Nathan and G. Burns, Phys. Rev. 129, 125 (1963).
16. R.S. Title, IBM J. Research Develop. 7, 68 (1963).
17. W.S. Baer and R.W. Dexter, Phys. Rev. 135, 1388 (1964).
18. K. Sawamoto, J. Phys. Soc. Japan 18, 1224 (1963).
19. G.D. Mahan and J.J. Hopfield, Phys. Rev. Letters 12, 241 (1964).
20. H. Fröhlick, Advances in Physics (Taylor and Francis, London, England, 1954) Vol.3, p.325.
21. A.R. Hutson, J. Appl. Phys. Suppl. 32, 2287 (1961).
22. J.O. Dimmock and A.J. Freeman, Phys. Rev. Letters 13, 750 (1964).
23. J.C. Slater, Phys. Rev. 51, 846 (1937); 92, 603 (1953).
24. Solid State Research Report, Lincoln Laboratory, M.I.T. (1963:4) p.48, DDC 435023.
25. H. Brooks, Advances in Electronics and Electron Physics (Academic Press, New York, 1955), Vol.7, p.153.
26. C. Herring and E. Vogt, Phys. Rev. 101, 944 (1956).
27. M.E. Fine, J. Appl. Phys. 26, 862 (1955).
28. T.C. Harman, W.H. Kleiner, A.J. Strauss, G.B. Wright, J.G. Mavroides, J.M. Honig, and D.H. Dickey, Solid State Commun. 2, 305 (1964).
29. T.C. Harman and A.J. Strauss, J. Appl. Phys. 32, 2265 (1961).
30. A.J. Strauss, T.C. Harman, J.G. Mavroides, D.H. Dickey, and M.S. Dresselhaus, Proceedings of the International Conference on the Physics of Semiconductors, Exeter (1962), p.703.

V. MAGNETISM AND RESONANCE

A. THEORETICAL

1. Determination of Ordering Temperatures from High-Temperature Expansions

Kramers and Opechowski[1] first suggested that one could estimate the Curie temperature from the high-temperature expansion for the zero-field susceptibility per particle $\chi(T)$ by using the definition that $\chi(T) \to \infty$ as $T \to T_c$. The susceptibility can accordingly be expressed as a power series in $\beta = (kT)^{-1}$, or more conveniently as

$$\chi(T) = \sum_{r=0}^{\infty} a_r \tau^r \tag{1}$$

where $\tau = T_M/T$, T_M being the ordering temperature estimated by the molecular-field approximation. Given a particular model, the first few terms of this series can be evaluated explicitly, and an estimation of its radius of convergence can be attempted. If the ratio test is used to obtain this estimate, one finds that $T_c = \rho T_M$, where $\rho = \lim_{n\to\infty} |a_{n+1}/a_n|$. If the ratios of successive pairs of terms are sufficiently well behaved, this estimate can be made with reasonable accuracy; otherwise it cannot.

We have carried out the necessary calculations for the case of a normal, cubic spinel possessing both A-B and B-B nearest-neighbor exchange interactions. We used the quantum-mechanical Heisenberg Hamiltonian and obtained $\chi(T)$ to fourth order in τ. The computed ratios are listed in Table V-1 for various values of the exchange parameter $u = (4J_{BB}S_B)/(3J_{AB}S_A)$. This method for estimating T_c is essentially that which Wojtowicz[2] has applied to the case of spinels with only A-B interactions, and indeed the successive ratios shown in Table V-1 for $u = 0$ appear to be reasonably well behaved. However, they become unmanageable when J_{BB} becomes appreciable, whether it is ferromagnetic ($u < 0$) or antiferromagnetic ($u > 0$). It is generally believed that the molecular field approximation overestimates the ordering temperature, usually by an appreciable amount. Thus, the results listed in Table V-1 for positive u preclude any possibility of obtaining even a crude approximation to T_c by this method.

In a recent paper,[3] we introduced the function defined by

$$\varphi(c, T) = N^{-1} \sum_{ij} c_i^* c_j \langle \underset{\sim}{S}_i \cdot \underset{\sim}{S}_j \rangle_T / (\bar{S}_i \bar{S}_j) \tag{2}$$

where $\bar{S}_i^2 = S_i(S_i + 1)$, S_i being the spin quantum number for the i^{th} site, and c denotes a set of c_i, which are constrained by

$$\sum_{ei} |c_i|^2 = N \quad . \tag{3}$$

Given the high-temperature expansion for the normalized spin correlation function $\delta_{ij} = \langle \underset{\sim}{S}_i \cdot \underset{\sim}{S}_j \rangle_T / (\bar{S}_i \bar{S}_j)$, one can write

TABLE V-1

RATIOS OF SUCCESSIVE COEFFICIENTS IN POWER SERIES REPRESENTATION OF MAGNETIC SUSCEPTIBILITY FOR $S_A = S_B = 3/2$

u	a_1/a_0	a_2/a_1	a_3/a_2	a_4/a_3
2.00	−2.743	−2.485	−2.349	−2.287
1.60	−2.279	−2.053	−1.959	−1.907
1.20	−1.870	−1.683	−1.614	−1.570
0.80	−1.513	−1.372	−1.308	−1.277
0.40	−1.205	−1.118	−1.031	−1.031
0.00	−0.943	−0.919	−0.772	−0.849
−0.40	−0.721	−0.775	−0.513	−0.791
−0.80	−0.535	−0.691	−0.239	−1.219
−1.20	−0.379	−0.681	0.056	5.261
−1.60	−0.250	−0.791	0.346	1.103
−2.00	−0.142	−1.191	0.581	0.856

TABLE V-2

RATIOS OF SUCCESSIVE COEFFICIENTS IN POWER SERIES REPRESENTATION OF CORRELATION OBTAINED WITH MOLECULAR-FIELD SPIN CONFIGURATIONS ($S_A = S_B = 3/2$)

u	a_1/a_0	a_2/a_1	a_3/a_2	a_4/a_3
2.00	1.000	0.493	0.541	0.046
1.60	1.000	0.627	0.597	0.443
1.20	1.000	0.732	0.668	0.657
0.80	1.000	0.810	0.732	0.770
0.40	1.000	0.864	0.784	0.829
0.00	1.000	0.899	0.821	0.858
−0.40	1.000	0.917	0.845	0.869
−0.80	1.000	0.925	0.857	0.869
−1.20	1.000	0.924	0.860	0.863
−1.60	1.000	0.918	0.857	0.853
−2.00	1.000	0.910	0.850	0.840

$$\varphi(c, T) = \sum_{r=0}^{\infty} a_r \tau^r \tag{4}$$

in analogy with Eq. (1). Each c (that is, set of c_i) represents a spin configuration, and the a_r of Eq. (4) depend upon this c. In effect, the function $\varphi(c, T)$ serves to project the spin correlations onto the configuration c. For example, if c is chosen so as to correspond to a ferromagnetic spin arrangement, then Eq. (4) becomes equivalent to Eq. (1).

However, we are concerned with finding the correction to the molecular-field ordering temperature T_M for a class of ferrimagnetic materials. In such a context, it would appear more reasonable to choose the c so as to represent the ferrimagnetic spin configuration computed in the molecular-field approximation for $T \cong T_M$. We have carried out this calculation up to order r = 4, and the ratios of the resulting a_r are listed in Table V-2 for the same set of u-values as before. We note first that, by virtue of the above construction, the initial ratio a_1/a_0 must always be unity. Then we note the general improvement of the behavior of successive ratios over that presented in Table V-1. There is significant improvement for u = 0; the improvement for nonzero u is pronounced. These new results are quite satisfactory for negative u, where the A-B and B-B interactions assist each other. Nevertheless, they deteriorate for sufficiently large, positive u, where the interactions compete strongly.

In the previous Solid State Research Report, we were primarily concerned with the problem of estimating the type of magnetic ordering to be expected at T_c from the behavior of $\tilde{c}$, where $\tilde{c}(T)$ was defined as that c which maximizes $\varphi(c, T)$ (Ref. 3). In other words, the configuration $\tilde{c}(T)$ possesses the largest possible projection of the spin correlations. The function $\varphi(\tilde{c}, T)$ can then be expressed as

$$\varphi(\tilde{c}, T) = \sum_{r=0}^{\infty} b_r \tau^r \tag{5}$$

which differs from the power series of Eq. (4) in that the implicit dependence of the original a_r upon T through their dependence upon the varying configuration $\tilde{c}(T)$ has been explicitly taken into account. Since $\varphi(\tilde{c}, T)$ is the maximum $\varphi(c, T)$, it must diverge the most strongly at T_c. Hence the estimation of a radius of convergence should follow most readily from the series given in Eq. (5).

The coefficients b_r have been computed up to order r = 4, and the resulting ratios are listed in Table V-3. The first two columns are identical with those of Table V-2 because the molecular-field solution constitutes the first approximation to $\tilde{c}(T)$, namely its temperature-independent term $\tilde{c}(\infty)$. However, the improvement in the behavior of the higher ratios is appreciable even for u = 0, and becomes large for very large u. For example, the modifications in the sequence of ratios for u = 1.6 are particularly striking, as one compares the different tabulations. We conclude that the use of the series for $\varphi(\tilde{c}, T)$ can greatly facilitate the estimation of a reliable value for T_c from a calculation of the first few terms of the high-temperature expansion for the spin correlation functions δ_{ij}.

K. Dwight
T. A. Kaplan
H. E. Stanley
N. Menyuk

TABLE V-3

RATIOS OF SUCCESSIVE COEFFICIENTS IN POWER SERIES REPRESENTATION OF OPTIMIZED CORRELATION ($S_A = S_B = 3/2$)

u	b_1/b_0	b_2/b_1	b_3/b_2	b_4/b_3
2.00	1.000	0.493	0.606	0.737
1.60	1.000	0.627	0.639	0.623
1.20	1.000	0.732	0.690	0.685
0.80	1.000	0.810	0.744	0.754
0.40	1.000	0.864	0.787	0.812
0.00	1.000	0.899	0.822	0.835
−0.40	1.000	0.917	0.844	0.850
−0.80	1.000	0.925	0.854	0.858
−1.20	1.000	0.924	0.857	0.856
−1.60	1.000	0.918	0.852	0.849
−2.00	1.000	0.910	0.846	0.839

2. Conduction-Electron Spin Density Induced by Localized Electrons

Recently, Overhauser and Stearns[4] have interpreted Mossbauer measurements[5] on Fe-Al alloys. They concluded that there is a large qualitative difference between the true 4s-electron susceptibility and the free-electron susceptibility $\chi_0(q)$, due to interactions between 4s electrons. [The free electron theory gives a 4s spin density S(R) which is in reasonable agreement with experiment for lattice points $R \neq 0$, but which is about an order of magnitude off at $R = 0$.] We have reconsidered the theory of the polarization of conduction electrons(s) by exchange interaction with localized electrons, neglecting s-s interactions. We note that the free-electron approximation gives conduction-electron wave-functions ψ_k proportional to $\exp[ik \cdot r]$ at the very center of the atomic core – obviously a poor approximation for interpreting hyperfine field measurements. We therefore took ψ_k as a plane wave orthogonalized to the core for determining the value of ψ_k at the nuclear positions. We found that although S(R) for $R \neq 0$ is essentially unchanged by this modification, S(0) is changed appreciably to be more in accord with experiment. These calculations show clearly that the conclusion of Overhauser and Stearns was premature, and that a theory neglecting s-s interactions might very well give reasonably good agreement with these experiments.

T. A. Kaplan

3. Chemical Inhomogeneities and Square B-H Loops

A paper of this title has been submitted to the Journal of Applied Physics. The abstract reads as follows:

"It is shown that in ferrites exhibiting spontaneously square B-H loops, reverse-domain nucleation may occur either at a grain boundary or at a chemical inhomogeneity having a volume roughly 0.1 a grain volume, a magnetization about 2 percent different from that of the parent matrix, and no static crystallographic discontinuity at the inhomogeneity-matrix interface. It is pointed out that such chemical inhomogeneities may occur in spinels having Jahn-Teller ions in concentrations that are too small to produce a cooperative, static distortion of the entire crystal from cubic symmetry. It is postulated that the formation of such inhomogeneities is responsible for the sharp knee in spontaneously square B-H loops found in many ferrites containing Mn^{3+} and Cu^{2+} ions, in particular the magnesium-manganese composition used in memory-core ferrites."

J. B. Goodenough

4. Energy-Level Scheme for $CoTiO_3$ and $FeTiO_3$

Previous DC susceptibility measurements of the effective moments of Co^{2+} and Fe^{2+} ions in $CoTiO_3$ and $FeTiO_3$, gave values of 5.47 and 5.21 Bohr magnetons for the respective ions. Based on a spin of 3/2 for Co^{2+} and 2 for Fe^{2+}, the spectroscopic splitting factors necessary to explain these moments are 2.83 and 2.13, respectively. Since the effective moment of $CoTiO_3$ is much greater than the spin-only value of 3.87 Bohr magnetons, there should be a substantial contribution of the orbital angular momentum to the moment, while in $FeTiO_3$ the measured moment exceeds the spin-only value (4.9 Bohr magnetons) by a much smaller amount and should have a smaller orbital angular momentum contribution.

It might have been anticipated from the anomalously large g-factor in $CoTiO_3$ that the crystal-field anisotropy would be greater in $CoTiO_3$ than in $FeTiO_3$. However, this is inconsistent with experiment. The dipole-dipole anisotropy favors spin alignment within the basal, c planes. In the case of $FeTiO_3$, the spins are directed along the c-axis, indicating a crystalline anisotropy greater than the dipole-dipole anisotropy. For $CoTiO_3$, the spins lie in the c-plane, indicating a crystalline-field anisotropy that is smaller than the dipole-dipole anisotropy.

These inconsistencies are partly resolved by considering the ground states of the ions, which in an octahedral field are triply degenerate, as being split under the action of spin-orbit coupling into a doublet ground state for $CoTiO_3$ ($J^* = 1/2$) with a $g^* = (13/3)$; and a triplet ground state for $FeTiO_3$ ($J^* = 1$), with a $g^* = 7/2$ (Ref. 6). In $CoTiO_3$, this will lead to an effective moment which will be particularly temperature dependent, since the excited states having $J^* = 3/2$ and 5/2 are separated from the ground state by (3/4) Λ and (2) Λ, respectively, where the Co^{2+} free-ion value of Λ is equal to 180 cm^{-1}. A calculation of the effective moments at temperatures of 60° and 120°K gives values of 5.25 and 5.05 for the respective moments, showing that for the temperature range over which the susceptibility was measured, the experimental moment exceeds the computed value by 10 percent at most.

The measured antiferromagnetic resonance frequency f_c for $CoTiO_3$, extrapolated to 0°K is 145 kMcps. With octahedral coordination and crystalline-field contribution to the anisotropy field neglected because of the doublet ground state, the resonance frequency at 0°K with no applied magnetic field is given by $f = e/2mc\,(g^*/2)\sqrt{2\Lambda(K_{||} - K_{\perp})}$, where $K_{||}$ and $K_{\perp}$ are the

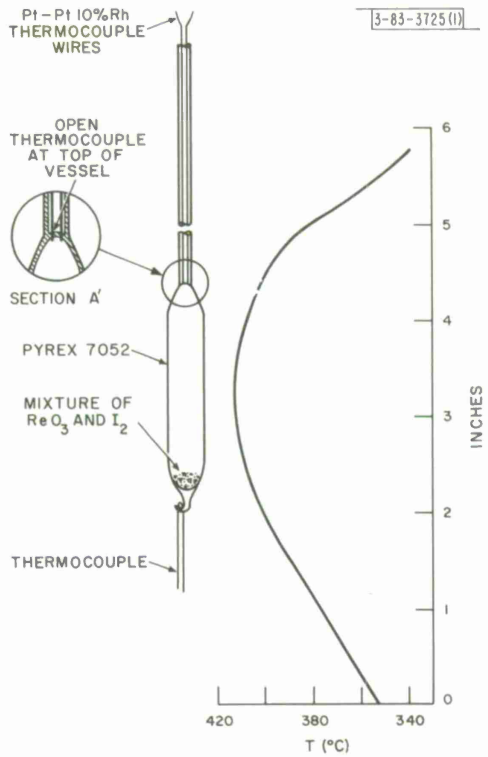

Fig. V-1. Modified ampoule and furnace temperature profile for vapor growth of ReO_3 crystals.

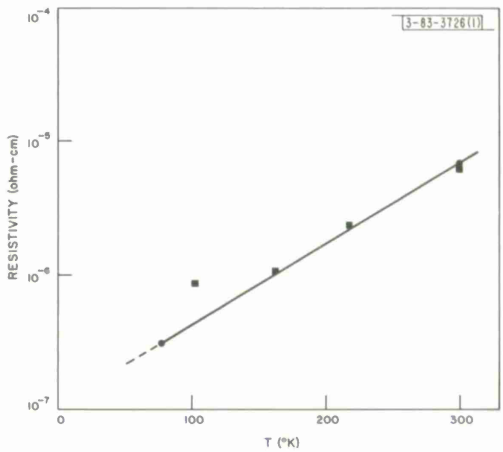

Fig. V-2. Temperature dependence of resistivity for an ReO_3 single crystal. Measurements made with two instruments using DC currents of 100 ma (•) and 2 amp (▪).

anisotropy energy constants for spins along and perpendicular to the c-axis. To satisfy the resonance frequency equation, g* must equal 3.56, which differs somewhat from the octahedral field value of 13/3. This indicates the presence of a trigonal-field component in addition to the octahedral.

A trigonal field acting on Co^{2+} will introduce no additional anisotropy in the ordered state since the ground state which is well separated from excited states has $J^* = 1/2$. However, in $FeTiO_3$, where the ground state has $J^* = 1$, a small trigonal field lifts the degeneracy only slightly and a considerable crystal field anisotropy is possible.

J. J. Stickler
J. B. Goodenough
H. J. Zeiger

B. EXPERIMENTAL

1. Crystal Growth and Electrical Properties of Rhenium Trioxide

Interest in the electrical properties of rhenium trioxide has been indicated in previous Solid State Research Reports.[7,8] It was shown that this material, when prepared by conventional techniques, is usually nonstoichiometric. However, effective purification was obtained via a vapor transport technique using iodine as transporter. In these experiments, transport of ReO_3 occurred in a two-zone furnace under conditions of high iodine vapor pressure in the direction of the cooler zone. These observations suggested the application of this technique to the growth of ReO_3 single crystals. Several preliminary experiments were based on the method described by Fischler[9] for the growth of tellurium-doped silicon crystals. This consists of growth from the vapor by slowly pulling a sealed ampoule containing the charge through a vertical gradient. Although these experiments indicated that the technique was in principle applicable, transport was not complete and the crystals obtained were too small for conductivity measurements. These results indicated that effective transport was very sensitive to the temperature differential between the reaction and crystallization ends of the ampoule and to the iodine pressure. Thus, the rate of pull was too rapid.

In order to establish the optimum conditions for crystal growth, the ampoule has been modified as shown in Fig. V-1. Platinum and platinum-10% rhodium thermocouple leads were sealed into the top of the ampoule in such a way that the unconnected ends extended about 1 mm into the ampoule and were about 0.5 mm apart. Externally, the leads were connected in series with a flashlight battery and bulb. With this arrangement the ampoule was again pulled slowly through the temperature gradient. As crystal growth began at the top of the ampoule, the deposited ReO_3 shorted the internal leads, completing the circuit as indicated by the glowing bulb. At this point, the pulling mechanism was stopped and the growth temperature determined by connecting the thermocouple leads to a potentiometer. The ampoule was maintained in this position for a period of 24 hours. Under these conditions, transport was complete and relatively large crystals (approximately 2.5 mm on an edge) suitable for conductivity measurements were obtained. The optimum crystallization temperature determined in this way appeared to be 370° ± 5°C with a temperature differential at the bottom of the ampoule of about 10° to 15°C.

Electrical resistivity values obtained on a typical ReO_3 single crystal are shown in Fig. V-2 as a function of temperature between 77° and 300°K. These values are remarkably low for

an oxide. The room-temperature resistivity is about one order of magnitude lower than that of the most highly conducting tungsten bronze and the 77° value is similar to that of electrolytically pure silver. In accordance with the premise previously stated,[7] these results for ReO_3 indicate that occupancy of the A-sites in oxides with perovskite or ReO_3 structures is not a necessary prerequisite for the formation of conduction bands in these materials.

A. Ferretti R. W. Germann
D. B. Rogers E. J. Delaney

2. The Effect of Trivalent Manganese on Crystal Chemistry of Some Lithium Spinels

The following is the abstract of an article that has been submitted to the Journal of Applied Physics:

> "Crystallographic properties of the spinel systems $Li_{0.5}Ga_{2.5-x}Mn_xO_4$ $(0 \leqslant x \leqslant 0.7)$, $Li_{0.5}Fe_{2.5-x}Mn_xO_4 (0 \leqslant x \leqslant 0.5)$, and $Li_{0.5}Al_{2.5-x}Mn_xO_4$ $(0 \leqslant x \leqslant 0.5)$ have been investigated in order to determine the effects of trivalent manganese substitutions on the crystal chemistry of the ordered spinel hosts. In each system relatively small concentrations of Mn^{+3} removed long-range ordering of lithium ions on the octahedral sites. This loss of order was accompanied by anomalies in the dependence of lattice parameters on composition. These observations can be qualitatively interpreted by assuming that Mn^{+3} ions tend to cluster in order to reduce the elastic energies associated with Jahn-Teller stabilizations. These effects may provide indirect evidence for lattice imperfections such as have been invoked to account for square B-H hysteresis loops in ferrite materials containing Jahn-Teller ions."

In the course of this discussion, it is pointed out that clusters of Mn^{+3} ions such as those envisaged are consistent with the mechanism for reverse domain nucleation assumed by Goodenough in a companion paper.

D. B. Rogers
R. W. Germann
R. J. Arnott

3. Phase Transitions in $LaCoO_3$

$LaCoO_3$ has been investigated by means of x-ray powder diffraction in the temperature range $500°K \leqslant T \leqslant 1600°K$ and by means of differential thermal analysis from room temperature to 1500°K. The two methods have consistently shown the existence of a first-order transition at 1210°K. Electrical measurements performed by previous authors indicate a sharp minimum in the resistivity at this temperature. Further measurements are required before a definitive interpretation of the peculiar magnetic, electrical, and crystallographic properties of this compound can be established.

P. M. Raccah
C. Anderson

4. Properties of B31 Compounds

In order to further examine the dependence of the signs of the magnetic couplings and the magnitude of the atomic moments of B31 compounds as a function of the electron/atom ratio,

crystallographic and magnetic studies of the systems $Fe_xMn_{1-x}P$ and FeP-FeAs-FeSb have been initiated.

Compounds of the system $Fe_xMn_{1-x}P$ were prepared by heating the elements in a sealed quartz tube to 1150°C at the rate of 20°C/hour. These compounds were held at this temperature for three days, slow cooled to 800°C and then quenched. Heating below 800°C for any time produces a phase separation. The unit cell decreases slightly with increasing x, each lattice parameter obeying Vegard's law. In the range of iron concentrations $0 < x < 0.25$, the metamagnetic transition temperature at 50°K in MnP increases with increasing x and the ferromagnetic Curie temperature T_c decreases slightly. The paramagnetic Curie temperature also decreases with increasing x. For larger x, there is only metamagnetism below the long-range magnetic-ordering temperature, the paramagnetic Curie temperature becoming $\Theta < T_c$ and continuing to decrease with increasing x. The Curie temperature becomes negative at $x = 0.55$ and reaches a minimum at $x \approx 0.8$. Iron phosphate is ferromagnetic with $\Theta \gtrsim T_c$, suggestive of a possible metamagnetic-ferromagnetic two-phase region occurring in the interval $0.8 < x < 1.0$.

J. B. Goodenough
W. A. Newman

5. Temperature Dependence of Attenuation of 70-Gcps Acoustic Waves in Quartz

With present techniques, experimental measurements using phonon generation at 70 Gcps are marginal. Two main areas are now being investigated that may lead to improved system performance. The area which offers the greatest possible gain is improvement of the over-all electromagnetic to acoustic transducing efficiency. Thin-film transducers of CdS or ferromagnetic films with a magnetic biasing field are presently available alternatives to single-surface generation of the quartz itself. Even if this approach does not yield improved efficiencies, it permits nonpiezoelectric materials to be measured. Another area of possible improvement is the reduction of the receiver noise figure from its present value of 18 db by using a different mixer configuration or by preceding the mixer with a klystron preamplifier.

The present system is also being modified to permit attenuation measurements to be made down to 1.5°K.

J. B. Thaxter
C. D. Parker
P. E. Tannenwald

REFERENCES

1. H.A. Kramers, Leiden Supplement No. 83, 1936 (unpublished), and W. Opechowski, Physica 4, 181 (1937); 6, 1112 (1938).
2. P.J. Wojtowicz, J. Appl. Phys. Suppl. 31, 265S (1960).
3. T.A. Kaplan, H.E. Stanley, K. Dwight and N. Menyuk, J. Appl. Phys. Suppl. (to be published).
4. A.W. Overhauser and M.B. Stearns, Phys. Rev. Letters 13, 316 (1964).
5. M.B. Stearns and S.S. Wilson, Phys. Rev. Letters 13, 313 (1964).
6. J.S. Griffith, The Theory of Transition-Metal Ions (Cambridge University Press, London, 1961).
7. Solid State Research Report, Lincoln Laboratory, M.I.T. (1964:2), DDC 606126.
8. Solid State Research Report, Lincoln Laboratory, M.I.T. (1964:3).
9. S. Fischler, "Vapor Growth and Doping of Silicon Crystals with Tellurium as Carrier," Metallurgy of Advanced Electronic Materials, G.E. Brock, ed., Metallurgical Society Conferences 19 (Interscience, New York 1963), p. 273.

DOCUMENT CONTROL DATA – DD 1473

1. ORIGINATING ACTIVITY Lincoln Laboratory, M.I.T.	2a. REPORT CLASSIFICATION Unclassified 2b. DOWNGRADING GROUP

3. REPORT TITLE

Solid State Research

4. TYPE OF REPORT AND INCLUSIVE DATES

Quarterly Progress Report, 1 October 1964 through 31 December 1964

5. AUTHOR(S) *(Last name first)*

Gatos, H.C.

6. REPORT DATE	7a. NO. OF PAGES	7b. NO. OF REFS.
15 January 1965	80	96

8a. CONTRACT NO. AF 19(628)-500	9a. ORIGINATOR'S REPORT NO. Solid State Research Report (1964:4)
8b. ORDER NO.	9b. OTHER REPORT NO(S). ESD-TDR-65-31

10. AVAILABILITY OR LIMITATION NOTICES

11. SUPPLEMENTARY NOTES	12. SPONSORING ACTIVITY Electronic Systems Division

13. ABSTRACT

This report covers in detail the solid state research work at Lincoln Laboratory. The topics covered are Solid State Device Research, Laser Research, Materials Research, Band Structure and Spectroscopy of Solids, and Magnetism and Resonance.

14. KEY WORDS

absorption, solid state physics, lasers, lead selenide, indium antimonide, ruby, mercury, crystal growth, sapphire, iodine, titanium, antimony, bismuth, germanium, gallium arsenide, silicon, manganese, lithium, spinels, attenuation, acoustic waves, spin, semi-metals, photons, superconductivity

Printed by
United States Air Force
L. G. Hanscom Field
Bedford, Massachusetts